

## MOLECULAR TRACERS OF THE CENTRAL 12 PC OF THE GALACTIC CENTER

MELVYN C. H. WRIGHT<sup>1</sup>, ALISON L. COIL<sup>1</sup>, ROBESON S. MCGARY<sup>2</sup>, PAUL T.P. HO<sup>2</sup> AND  
ANDREW I. HARRIS<sup>3</sup>

*To appear in The Astrophysical Journal*

### ABSTRACT

We have used the BIMA array to image the Galactic Center with a 19-pointing mosaic in HCN(1-0), HCO<sup>+</sup>(1-0), and H 42 $\alpha$  emission with 5 km s<sup>-1</sup> velocity resolution and 13''  $\times$  4'' angular resolution. The 5' field includes the circumnuclear ring (CND) and parts of the 20 and 50 km s<sup>-1</sup> clouds. HCN(1-0) and HCO<sup>+</sup> trace the CND and nearby giant molecular clouds while the H 42 $\alpha$  emission traces the ionized gas in Sgr A West. We find that the CND has a definite outer edge in HCN and HCO<sup>+</sup> emission at  $\sim$  45'' radius and appears to be composed of two or three distinct streams of molecular gas rotating around the nucleus.

Outside the CND, HCN and HCO<sup>+</sup> trace dense clumps of high-velocity gas in addition to optically thick emission from the 20 and 50 km s<sup>-1</sup> clouds. A molecular ridge of compressed gas and dust, traced in NH<sub>3</sub> emission and self-absorbed HCN and HCO<sup>+</sup>, wraps around the eastern edge of Sgr A East. Just inside this ridge are several arcs of gas which have been accelerated by the impact of Sgr A East with the 50 km s<sup>-1</sup> cloud.

HCN and HCO<sup>+</sup> emission trace the extension of the northern arm of Sgr A West which appears to be an independent stream of neutral and ionized gas and dust originating outside the CND. Broad line widths and OH maser emission mark the intersection of the northern arm and the CND.

Comparison to previous NH<sub>3</sub> and 1.2mm dust observations shows that HCN and HCO<sup>+</sup> preferentially trace the CND and are weaker tracers of the GMCs than NH<sub>3</sub> and dust. We discuss possible scenarios for the emission mechanisms and environment at the Galactic center which could explain the differences in these images.

*Subject headings:* galaxies: The Galaxy — Galaxy: center — techniques: interferometric — ISM: molecules

### 1. INTRODUCTION

A 2-5 pc circumnuclear ring (CND) of neutral gas and dust has been imaged at the Galactic Center in the far-infrared and radio (Genzel et al. 1985; Güsten et al. 1987; Marr, Wright, & Backer 1993). It has been proposed that the CND is part of an accreting disk of material surrounding the massive central source Sgr A\* (Güsten et al. 1987), an apparent supermassive black hole (Ghez et al. 1998; Genzel et al. 1997). Ionized gas streamers appear to be infalling towards the central mass, originating at the inner edge of the CND and converging at the location of the bar near Sgr A\* (Lo & Claussen 1983). It is unclear whether the CND is a transitory or stable structure. If it is stable, the question remains as to how the CND itself is maintained.

At a projected distance of 10 pc from the Galactic Center lie two giant molecular clouds (GMC), the 20 km s<sup>-1</sup> cloud (M-0.13-0.08) and the 50 km s<sup>-1</sup> cloud (M-0.02-0.07) (Güsten, Walmsley, & Pauls 1981) to the south and east of the CND respectively. Güsten & Downes (1981) argued that these clouds must lie more than 100 pc from the Galactic Center in order not to be tidally disrupted. Their interpretation of formaldehyde absorption data places the 50 km s<sup>-1</sup> cloud behind the nucleus and the 20 km s<sup>-1</sup> cloud in front. Various studies have investigated the interactions between these molecular clouds, the non-thermal

radio source Sgr A East, the CND and the ionized gas streamers in the nucleus (Ho et al. 1985; Genzel et al. 1990; Ho et al. 1991; Serabyn et al. 1992; Dent et al. 1993; Marshall, Lasenby, & Harris 1995; Coil & Ho 2000). There are suggestions of molecular gas streamers from both of the GMCs located 10 pc away in projection that may be feeding the CND. A southern streamer has been mapped in NH<sub>3</sub>(1,1), (2,2) and (3,3) and sub-millimeter continuum (Ho et al. 1991; Dent et al. 1993; Coil & Ho 1999) and emission in the same region has been seen in HCN(3-2) (Marshall, Lasenby, & Harris 1995). An eastern streamer, lying at the edge of the Sgr A East SNR and protruding in towards the nuclear region, has been mapped in HCN(1-0) (Ho 1993) and HCN(4-3) and HCN(3-2) (Marshall, Lasenby, & Harris 1995). This streamer has not been seen in NH<sub>3</sub> or sub-millimeter continuum. More recently, Coil & Ho (2000) presented images of two streams of NH<sub>3</sub>(1,1) and (2,2) emission parallel to the Galactic plane, which they interpret as evidence for infall from the 20 km s<sup>-1</sup> cloud onto the CND, and as evidence for interactions between Sgr A East and the 50 km s<sup>-1</sup> cloud, and a SNR to the south of Sgr A East (G359.92-0.09). They argue that both clouds are within 10 pc of the nucleus and that only the 20 km s<sup>-1</sup> cloud is interacting with the CND.

Many of these observations have a limited field-of-view and velocity coverage, mapping only the central 2 – 4' (5–10pc) of the Galaxy and not extending into the large

<sup>1</sup> Radio Astronomy Laboratory, University of California, Berkeley, CA 94720 E-mail: mwright@astro.berkeley.edu, acoil@astro.berkeley.edu

<sup>2</sup> Harvard-Smithsonian Center for Astrophysics, 60 Garden St., Cambridge, MA 02138 E-mail: rmcgary@cfa.harvard.edu, ho@cfa.harvard.edu

<sup>3</sup> University of Maryland, E-mail: harris@astro.umd.edu

molecular clouds, thereby unable to thoroughly address the question of possible interactions with the circumnuclear region. This paper describes observations with the BIMA array<sup>4</sup> of the central 5' in HCO<sup>+</sup>, HCN(1-0), and H 42 $\alpha$  emission with 5 km s<sup>-1</sup> resolution, and in 87 GHz continuum emission. The 5' field of view corresponds to a field roughly 12.5 pc at the distance of the Galactic Center (assuming  $R_{\odot} = 8.5$  kpc).

## 2. OBSERVATIONS

Observations were obtained with the BIMA array (Welch et al. 1996) between 1998 March and 1999 October using four antenna configurations with antenna separations from 6 to 240m, including the recently completed, compact D-array which gives good  $uv$  coverage down to the 6.1 m antenna diameter, and a new C-array which greatly improves the  $uv$  coverage for low declination sources. Figure 1 shows the  $uv$  coverage. The resulting synthesised beam width (FWHM) is  $13.2'' \times 4.3''$ .

We mapped the Galactic Center simultaneously in HCN (J=1-0), HCO<sup>+</sup> (J=1-0), and H 42 $\alpha$  emission with 5 km s<sup>-1</sup> resolution over a velocity range of 300 km s<sup>-1</sup> centered close to  $v_{LSR} = 0$  km s<sup>-1</sup> for all three spectral lines. We also mapped 87 GHz continuum emission with 400 MHz bandwidth in each sideband of the local oscillator. We used a 19-pointing hexagonal mosaic with 1' spacing centered on Sgr A\*. Additional observations were obtained in a single pointing centered on Sgr A\* to enhance the sensitivity to emission within the central 2' and to compare with the images obtained from the mosaic observations.

We observed the quasar 1733-130 as a phase calibrator at 30 to 35 min intervals after 2 complete cycles of 19 pointings with 35 s observations at each pointing. This cycle of observations was repeated for 4 to 5 hours while the Galactic Center was above  $\sim 12^{\circ}$  elevation. Uranus was observed to check the flux density calibration, and the strong quasar 3C273 was used for the bandpass calibration. The flux density scale is accurate to about 10%, and the on-line bandpass calibration is good to about 5%. The data were calibrated and imaged using the MIRIAD software package (Sault Teuben & Wright 1995).

## 3. IMAGE FIDELITY

In order to estimate the errors in our images, we processed the data in a number of different ways and compared the resulting images. Images using different subsets and weightings of the  $uv$  data are consistent to about 5% RMS of the peak value.

Single sideband system temperatures during the observations ranged from 170 to 1600 K scaled to outside the atmosphere. Images were made by weighting the  $uv$  data by the inverse square of the system temperature. Robust weighting was used as a compromise between natural weighting, which gives the lowest thermal noise, and uniform weighting of the  $uv$  plane.

We deconvolved the images using both the SDI CLEAN algorithm (Steer, Dewdney & Ito 1984), and the maximum entropy algorithm (MEM) (Sault Staveley-Smith & Brouw 1996). To avoid bias in the MEM images, we used an entropy measure  $-\log(\cosh(p))$  – also called the maximum emptiness criteria, where  $p$  is the pixel value. This

entropy measure handles the complex regions of emission and absorption seen in the spectral line images. Images of individual pointings are consistent with the mosaic images.

The noise level varies with radius in the mosaic images. For the spectral line images, the thermal noise level is 0.07 K in 20 km s<sup>-1</sup> channels at the map center, increasing to 0.11 K at 120'' radius and 0.15 K at 150'' radius. We compared spectral line images obtained by interchanging the order of velocity averaging, deconvolution, and continuum subtraction. The 20 km s<sup>-1</sup> images are consistent with an RMS difference over the central 5' field of 0.1-0.2 K, and a maximum difference (between 120'' and 150'' radius) of 0.7 K. At the 5 km s<sup>-1</sup> resolution in the spectra which follow, the measured rms noise level is around 0.5 K in a  $13.2'' \times 4.3''$  synthesised beam, giving a dynamic range of about 20:1. We also compared images of the 85 and 89 GHz data in each sideband of the local oscillator. The rms difference between these images is 35 mJy with a maximum difference of 100 mJy. The theoretical thermal noise in the difference image is 25 mJy.

### 3.1. Data Sampling

The hexagonal pointing mosaic with 1' spacing is well sampled at 89 GHz (with a primary beam FWHM of 2.15'), giving images with approximately uniform sensitivity across a 5' field. For a mosaic with 19 pointing positions, the Nyquist sample interval is 9 s on the maximum 240 m baseline used in these observations. Our 35 s sample interval was chosen to minimize the overall noise in the images, taking into account the observing efficiency and the data sampling. Repeated observations of each  $uv$  track (Figure 1) extend the Nyquist sampling of the data along the  $uv$  tracks to 100 m (30 k $\lambda$ ) baselines, as well as fill in many calibration gaps. Compact structures are adequately sampled out to the maximum 240 m (75 k $\lambda$ ) baseline. Extensive modeling of mosaic images with undersampled data (Wright 1999) shows a slow degradation of image fidelity with decreasing sampling.

### 3.2. Missing Short Spacings

These images do not include any observations shorter than the minimum interferometer spacing of 6.1 m. The missing short spacings contain information about structures larger than about 1'. Both SDI and MEM deconvolutions are very similar if we use an entropy measure  $-\log(\cosh(p))$ . For the HCN and HCO<sup>+</sup> emission, which are heavily absorbed by foreground gas, the spatial filtering provided by the interferometer is an advantage in isolating warmer material associated with the CND, but resolves out the large scale structure of the nearby molecular clouds.

In summary, structures with angular scales between 1' and the  $13'' \times 4''$  resolution are well sampled in these images, giving an image fidelity close to the thermal noise, or 5% of the peak value in each spectral channel, whichever is greater.

## 4. RESULTS

### 4.1. Continuum Emission

<sup>4</sup> The BIMA array is operated by the Berkeley-Illinois-Maryland Association under funding from the National Science Foundation.

Figure 2 shows 87 GHz continuum emission over an 800 MHz bandwidth averaged over line-free spectral windows in both sidebands of the local oscillator. We imaged the eight 100 MHz continuum bands in both sidebands of the local oscillator and found that the images were consistent. We then averaged the upper and lower sidebands separately. These two images agree within an 8% scale factor and 14 mJy rms, consistent with calibration errors (10%) and thermal noise (13 mJy/beam) respectively. The upper and lower sidebands were combined to produce the image shown in Figure 2. In this and the following mosaic images, the primary beam attenuation is fully corrected out to  $150''$  radius, falling to 0.5 at  $180''$ . This attenuation can be seen in the contours in Figure 2. The rms noise level in the averaged continuum image is 6 mJy/beam at the center, increasing to 13 mJy/beam at  $150''$  radius. Within the  $5'$  field we can see the thermal mini-spiral, the central bar, the western arc curving around to the southwest, and the non-thermal emission from Sgr A\* (see Lacy et al. 1991 Figure 1 for a discussion of features in the mini-spiral). The features at  $\sim 100''$  north and south are alias responses resulting from the discrete  $uv$  sampling.

The SDI and MEM deconvolutions result in an integrated flux density out to  $30''$  of 8.9 Jy and 14.2 Jy, respectively. The integrated flux density estimated from the shortest  $uv$  spacings (6.1 m) is  $15 \pm 1$  Jy, with considerable structure apparent on arcmin scales. The MEM deconvolution has recovered most of the flux density observed on the shortest interferometer spacings, but falls short of the  $\sim 27$  Jy obtained with single dish observations (Wright & Backer 1993). The peak flux density is 2.14 Jy/beam and includes emission from both Sgr A\* and the region of the bar a few arcseconds to the south. The average flux density of Sgr A\* itself, estimated from both the  $uv$  data and the image deconvolution, is 1.7 to 1.8 Jy/beam, which is consistent with previous observations of Sgr A\* at this resolution (Wright & Backer 1993). Although the flux density of Sgr A\* may have varied during the observations, the present data do not include sufficiently long  $uv$  spacings to reliably estimate this.

Gaussian fits to the compact continuum emission ( $180''$  east,  $60''$  north) give a peak flux density of 160 mJy/beam and an integrated flux density of 510 mJy with an overall error of  $\sim 10\%$  (after correction for the residual primary beam attenuation). The fitted position is  $\alpha_{2000} = 17^h 45^m 52^s.05$ ,  $\delta_{2000} = -28^\circ 59' 30''.91$ , consistent with a blend of two compact sources, Sgr A-A and Sgr A-B, with a total flux density of 337 mJy at  $\lambda = 6$  cm (Ho et al. 1985). These sources are in a string of compact HII regions with shell-like structures located to the east of the Sgr A East shell (Ekers et al. 1983; Goss et al. 1985; Yusef-Zadeh & Morris 1987).

#### 4.2. H 42 $\alpha$ Emission

Figure 3 shows the H 42 $\alpha$  emission integrated from  $-150$  to  $+150$  km s $^{-1}$ . This image was formed by first subtracting the lower sideband continuum image from the H 42 $\alpha$  spectral channels averaged in 20 km s $^{-1}$  intervals, and then averaging the SDI deconvolution of these images. The H 42 $\alpha$  emission traces the same thermal continuum emission as Figure 2. The western arc is clearly resolved, but the northern arm and bar are blended together at this angu-

lar resolution. Figure 4 shows the H 42 $\alpha$  spectra at 20 km s $^{-1}$  resolution for the positions marked in Figure 3. H 42 $\alpha$  emission extends over the full velocity range sampled. Emission at high positive velocities is seen in the central bar close to Sgr A\* (spectrum A), while the northern arm is prominent from  $+50$  to  $+150$  km s $^{-1}$ , the upper edge of the spectral window (spectrum B). Emission from the western arc extends from  $-50$  to  $-150$  km s $^{-1}$ , the lower edge of the window (spectra C and D). Our H 42 $\alpha$  image is consistent with the H 92 $\alpha$  emission described in detail by Roberts & Goss (1993).

#### 4.3. Molecular Emission

Figure 5 shows the deconvolved images of HCN(1-0) emission in 20 km s $^{-1}$  intervals, made by subtracting the upper sideband continuum image from 20 km s $^{-1}$  averages of HCN(1-0) spectral channels and then deconvolving these 20 km s $^{-1}$  images. The rotating circumnuclear ring (CND) can be seen at a radius of  $\sim 30''$  to  $60''$  in many channels and is most obvious as the arc-like structures  $40''$  south at a velocity of  $-70$  km s $^{-1}$  and  $40''$  north at velocities of 70 and 90 km s $^{-1}$ . Features associated with nearby GMCs are also visible. At 30 km s $^{-1}$ , emission at the southern edge of the image ( $-100''$  to  $-140''$ ) is associated with the 20 km s $^{-1}$  cloud. A north-south ridge of emission at 30-90 km s $^{-1}$ , located  $120''$  to the east, traces gas compressed by the expansion of Sgr A East into the 50 km s $^{-1}$  cloud (Serabyn et al. 1992).

HCO $^+$  emission in 20 km s $^{-1}$  intervals, made in the same way as the HCN(1-0) images, is shown in Figure 6. The HCO $^+$  and HCN(1-0) emission trace the same features, though the HCO $^+$  emission is generally weaker. A prominent feature in HCN(1-0) which is *not* seen in HCO $^+$  is the “70 km s $^{-1}$  cloud” apparent from 30 km s $^{-1}$  to 70 km s $^{-1}$  on the western edge of the CND.

Figure 7 presents a comparison of HCN(1-0) and HCO $^+$  in the central 15 pc of the Galaxy. Contours of velocity-integrated HCN(1-0) emission spanning  $-150$  km s $^{-1}$  to  $+150$  km s $^{-1}$  are superposed on the background of HCO $^+$  emission in the same velocity range. The integrated HCN emission is essentially the same as the HCO $^+$ , except for deeper absorption features in the HCO $^+$ . The CND is seen as an almost complete ring with two opposing lobes of strong emission, surrounded by lower-level, clumpy emission.

Our results are fully consistent with earlier observations of the CND at similar resolution (Güsten et al. 1987; Marr, Wright, & Backer 1993). Emission from the CND is from warm ( $T \sim 150 - 450$  K), clumpy gas with molecular density  $\sim 10^5 - 10^6$  cm $^{-3}$  (Genzel et al. 1985). HCN and HCO $^+$ (1-0) are both optically thick and have similar excitation requirements and should have similar distributions apart from chemistry, shock and ionization effects. While both HCN(1-0) and HCO $^+$  trace gas with a molecular density  $\sim 10^5 - 10^6$  cm $^{-3}$ , HCO $^+$  has a larger collision cross section and is subject to greater absorption along the line of sight.

Figure 8 marks positions of HCN(1-0) and HCO $^+$  spectra shown in Figures 9 and 10. Spectrum A, at the location of Sgr A\*, shows several absorption features. The narrow features at  $-30$ ,  $-50$ , and  $-135$  km s $^{-1}$  are thought to be due to galactic rings or arms at radii of 4 kpc (Menon &

Ciotti 1970), 3 kpc (Oort 1977), and 250 pc (Scoville 1972; Listz & Burton 1978; Bieging et al. 1981). The absorption from  $-10$  to  $+70$  km s $^{-1}$  suggests that the 20, 50 and 70 km s $^{-1}$  gas clouds in the Galactic Center region extend in front of Sgr A\*.

Several other spectra not near Sgr A\* also show absorption dips (e.g. R, S, T, U, V & X). These absorption features may be due to intervening gas or self-absorption. However, negative features also appear in the spectra as a result of undersampling of the data in the  $uv$  plane. As seen in Figures 5 & 6, there are artificial negative features surrounding structures on scales greater than  $60''$ , particularly at velocities from 10 to 90 km s $^{-1}$  where emission from the extended molecular clouds is partially resolved. However narrow self-absorption features corresponding to the 20, 50 and 70 km s $^{-1}$  clouds can be identified in many of the HCN and HCO $^+$  spectra.

## 5. DISCUSSION

The origin of the CNB is unclear. The central 2 arcminutes may have been swept clear of molecular material by a wind from the central black hole or correlated supernovae explosions (see a recent review by Morris & Serabyn 1996 and references therein). The CNB may also be fed from outside the nucleus with gas from nearby GMCs. It is also not understood whether the CNB is a long-lived or a transient feature. As seen in Figures 7 and 8 as well as in Genzel et al. (1985), Güsten et al. (1987) and Marr, Wright, & Backer (1993) the CNB is not a complete ring and lacks emission in the southeast. This gap could be due to intervening gas along the line of sight or could reflect an intrinsic lack of material in the region. If the CNB consists of several distinct streamers in general rotation around the nucleus, it is possible that the gas fell towards the center from farther away, creating a disk or ring structure which is not necessarily a stable or long-term feature. These observations probe the spatial extent and kinematics of the central 5' surrounding the nucleus. By determining if the CNB has a well-defined sharp outer edge, we can limit theories on its formation. In addition, the kinematic information can show if the CNB is a coherent feature or composed of distinct clouds.

### 5.1. Spatial Extent of the CNB

HCN and HCO $^+$  emission is seen across the entire field of Figure 7, however the CNB itself stands out clearly in the center. The inner edge of the CNB is well-delineated by the central cavity surrounding Sgr A\* and Sgr A West. The outer edge of the CNB is less sharply defined than in earlier single-pointing images (Genzel et al. 1985; Güsten et al. 1987; Marr, Wright, & Backer 1993) which are attenuated by the primary beam cutoff, but there still appears to be an outer edge. Figure 11 shows a radial profile of HCN(1-0) emission averaged around elliptical annuli. Following the steep rise from the center, there is a bright narrow ring peaked at  $\sim 45''$  radius. The average brightness of the emission quickly drops from  $45''$  to  $80''$  indicating that the CNB is a ring rather than a disk.

CO studies (Lugten et al. 1986, Harris et al. 1985) of this region show emission out to  $140''$  to the northeast and southwest, along the major axis of the ring, which appears to follow the general rotation pattern of the CNB.

In Figures 5 & 6, images from  $-130$  to  $-110$  km sec $^{-1}$  show emission from the southwest lobe of the CNB extending to  $120''$ . Position velocity cuts  $b$ ,  $c$  and  $e$  also show high-velocity HCN emission at  $\sim 100''$  to the southwest of the CNB. This emission has broad linewidths ( $\sim 60$  km s $^{-1}$ ) and may represent either a continuation of the CNB or a high-velocity streamer in this direction. However, there is no comparable extension of the northeast lobe. There is instead gas at  $+50$  to  $+90$  km sec $^{-1}$  associated with the expansion of Sgr A East, which has swept up and compressed gas in the  $50$  km sec $^{-1}$  cloud into a distinct streamer located  $150''$  from the nucleus. This asymmetry along the major axis may account for some of the earlier disagreements in the apparent rotation curve derived from lower resolution observations (e.g. see figure 7 in Güsten et al. (1987)).

In all other directions, there is a noticeable *lack* of emission outside  $50''$ , especially along the eastern edge between  $60''$  and  $80''$  radius. Far from the CNB, weak filamentary structures dominate the HCN and HCO $^+$  emission. As discussed below in section 5.5, absorption effects are important in the GMC's, so that the fall-off in the radial distribution is not as severe as shown in figure 11 in these directions. To the west, the "70km s $^{-1}$  cloud" does not fit the rotation pattern, and  $100''$  to the east there are large velocity gradients in the opposite sense to the CNB rotation. In addition, position velocity cut  $b$  shows clumps to the north of the CNB at  $-15$  and  $+70$  km s $^{-1}$  (see also spectrum M in Figure 9) which do not follow the rotation pattern of the CNB. We therefore conclude that the CNB is not a disk, but rather a ring with a definite outer edge in HCN(1-0) and HCO $^+$  emission.

### 5.2. Kinematics of CNB

Kinematically, the central 2' is largely consistent with a rotating ring of molecular gas with a peak at a radius of  $\sim 45''$ . The signature of the rotation is clearly seen in the spectral peaks at 75 and 100 km s $^{-1}$  at positions B and C to the northeast, and at  $-97$  km s $^{-1}$  at position I to the southwest. Coherent rotation cannot account for all of the spectral features seen in the CNB (see spectra E, G and H). To better address the question of coherent structure and rotation in the CNB, we present in Figure 12 a position-velocity diagram of emission around an ellipse with a major axis of  $40''$ , an inclination of  $60^\circ$ , and a position angle of  $25^\circ$  showing emission from the CNB only. The CNB is not a complete ring, with a noticeable lack of emission in the southeast, corresponding to  $\Theta \sim 60^\circ$  in the velocity range  $+60$  to  $-10$  km s $^{-1}$ . The CNB appears to consist of either two or three distinct streamers rotating around the nucleus. The southwest lobe of the CNB is seen in the top middle of the position-velocity diagram, between  $\Theta=50^\circ$  to  $250^\circ$  and velocity range  $-10$  to  $-130$  km s $^{-1}$ . The northeast lobe of the CNB is seen in the lower half of the image from  $\Theta=0^\circ$  to  $60^\circ$  and  $\Theta=325^\circ$  to  $360^\circ$  in the velocity range  $+50$  to  $+170$  km s $^{-1}$ . There is a third, possibly distinct feature, from  $\Theta=160^\circ$  to  $325^\circ$  in the velocity range  $+0$  to  $+125$  km s $^{-1}$ . This feature may or may not be a continuation of the southwest lobe. The small northern gap at  $\Theta \sim 220^\circ$  and  $0$  km s $^{-1}$  is discussed in the next section.

Previous suggestions have been made that the CNB is

a warped ring with inclination angles  $70^\circ$  and  $50^\circ$  for the southwest and northeast lobes respectively. The warped structure and the high velocity dispersion lead to a short dynamical lifetimes of  $10^4 - 10^5$  years (Güsten et al. 1987). Jackson et al. (1993), propose that the CNB is composed of several dynamically distinct streamers rotating around the nucleus. In this case, the two bright lobes are at different inclinations because they are on separate orbits. The morphological incompleteness of the ring as seen in our HCN(1-0) and HCO<sup>+</sup> data, along with the evidence for separate streamers seen in our position-velocity diagram of gas around the CNB, support the thesis of Jackson et al. (1993).

### 5.3. Infall from the North

While there is widespread HCN and HCO<sup>+</sup> emission throughout the central  $200''$ , there is also a conspicuous lack of emission in the northwest quarter of the image (at positive galactic latitude), where little dust or gas has been seen before. It seems that any prior material in this region has largely been swept clear, either from an outflow possibly related to the nucleus, or through accretion towards the center.

Figure 3 shows a distinct, narrow gap in HCN(1-0) and HCO<sup>+</sup> velocity-integrated emission in the northern part of the CNB exactly along the northern arm of the minispiral. The HCN and HCO<sup>+</sup> spectra to the east of this gap (spectrum C in Figures 9, 10) peak at  $100 \text{ km s}^{-1}$  with a FWHM of  $45 \text{ km s}^{-1}$  which match those in the ionized gas (Roberts & Goss 1993, Figure 11c). To the west of the gap (spectrum D), the spectra peak at  $\sim 70 \text{ km s}^{-1}$  with a comparable FWHM. These linewidths are roughly twice that of spectra on either side in the CNB (spectra B and F). The increase in the linewidth of the gas, along with the lack of negative contours, indicates that the gap is not due to absorption by gas in front of the CNB. Therefore, the gap seen in the velocity integrated map is a real feature of the CNB.

A 1720 MHz OH maser from collisionally excited gas behind a C-type shock (Yusef-Zadeh et al. 1999) is located in the gap (position X in Figure 3). The increase in linewidth of the gas near the gap in addition to the complete lack of HCN(1-0) and HCO<sup>+</sup> emission in the gap and the presence of the OH maser indicate that material is interacting with the CNB at this location. The superposition of the northern arm with the gap (see Figure 3) suggests that the northern arm crosses the CNB at this point.

It appears that the inflow of material began outside the CNB and disrupted the ring as it fell inward rather than originating from cloud-cloud collisions in the CNB itself. The HCN and HCO<sup>+</sup> emission west of the gap extends north to more than  $100''$  radius (Figure 7) beyond the CNB. Figure 13 shows position-velocity diagrams taken from cuts marked in Figure 8. Cut *c* shows that the spur to the north continues at the velocity of the northern arm of ionized gas. In a model of the far-IR structure at 31.5 and 37.7 micron (Latvakoski et al. 1999), the northern arm is on a parabolic orbit  $10^\circ$  from the plane of the CNB and extends 1.4 pc to the northwest of the CNB, suggesting that the northern arm is a separate stream of gas and dust which intersects the CNB as it falls in towards the center.

### 5.4. Interaction of Molecular clouds with Sgr A East

The HCN and HCO<sup>+</sup> images in Figures 5 and 6 show several structures outside the CNB. From  $-90$  to  $+90 \text{ km s}^{-1}$  there is emission throughout the eastern region of the images which may be associated with the  $50 \text{ km s}^{-1}$  cloud. There are absorption dips at both  $50$  and  $70 \text{ km s}^{-1}$  in the spectra to the northeast, and also to the southwest in spectra R, S, and T. Evidently the  $50$  and  $70 \text{ km s}^{-1}$  clouds extend over much of the Galactic center, as also indicated by large scale imaging of CS J=1-0 emission (Tsuboi Handa & Utika 1999). CS J=1-0 is a good tracer of dense molecular gas ( $n \sim 10^4 \text{ cm}^{-3}$ ). Tsuboi's Figures 3 and 4 show that the CS emission at  $50$  to  $70 \text{ km s}^{-1}$  extends over most of the Galactic center. In the HCN and HCO<sup>+</sup> images, there is extensive evidence of interaction of Sgr A East with the  $50 \text{ km s}^{-1}$  cloud to the east; to the west, outside of the CNB, there is little high-velocity HCN and HCO<sup>+</sup> emission, except for an isolated emission feature at  $-130 \text{ km s}^{-1}$  located  $156''$  west,  $52''$  south (spectrum W), and HCN emission at  $-60 \text{ km s}^{-1}$  located  $30''$  west,  $30''$  north (spectrum E). Blue-shifted C+ emission at the latter location indicates a substantial UV flux density and proximity to the Galactic center, and corresponds to the northwest edge of Sgr A East (Lugten et al. 1986).

A number of studies show that Sgr A East is expanding into the  $50 \text{ km s}^{-1}$  cloud (Mezger et al. 1989; Zylka, Mezger & Wink 1990; Genzel et al. 1990; Ho et al. 1991; Serabyn et al. 1992; Coil & Ho 2000). Serabyn et al. (1992) mapped a dense molecular ridge in CS J=7-6 and 5-4 emission, which wraps around the eastern side of Sgr A East. Figure 16 shows that NH<sub>3</sub> emission also closely follows the eastern edge of Sgr A East (Coil & Ho 2000). High velocity red- and blue-shifted emission is seen along the ridge in CS, HCN(1-0) and HCO<sup>+</sup>. Figures 5 & 6 show blue-shifted emission at  $-50$  to  $-90 \text{ km s}^{-1}$  located  $\sim 90''$  east and  $\sim 20 - 40''$  north, and at  $-50$  to  $-30 \text{ km s}^{-1}$  in the arc of emission in northern part of the images at  $90''$  east and  $140''$  north. Red-shifted emission is seen at  $+90$  to  $+110 \text{ km s}^{-1}$  along the molecular ridge, with the highest velocities at  $100''$  east and  $40''$  south. In Figure 16 the high-velocity emission, comprised of several clumps of gas, generally lies inside the molecular ridge of compressed gas imaged in CS J=7-6 and J=5-4 (Serabyn et al. 1992). Serabyn et al. argue that the high-velocity gas has been accelerated by the impact of Sgr A East with the  $50 \text{ km s}^{-1}$  cloud. Since both red- and blue-shifted gas is observed, parts of the  $50 \text{ km s}^{-1}$  cloud must lie on both the front and back side of the Sgr A East expanding shell. Spectra K, L, N, O, and Q show the high-velocity emission from this region. Clumps of HCN and HCO<sup>+</sup> emission, with steep velocity gradients (e.g. spectra O and Q at  $-80$  and  $+100 \text{ km s}^{-1}$  respectively), are superposed on the smoother, highly resolved ambient cloud material at  $20$  to  $60 \text{ km s}^{-1}$  with more modest velocity gradients of  $5-8 \text{ km s}^{-1} \text{ arcmin}^{-1}$  (see position-velocity profile *b* in Figure 13). These data suggest that clumps of gas have been compressed and accelerated as Sgr A East has expanded into the ambient cloud material. The ambient cloud material is self-absorbed in HCN and HCO<sup>+</sup> emission, indicating warmer gas overlaid by colder gas.

Figure 16 marks the positions of OH (1720) masers detected close to the Galactic Center superposed on an image

of 6 cm continuum emission which shows the Sgr A East shell. These 1720 MHz masers, which are seen without the main transitions, are usually associated with the interaction of expanding supernova shells with molecular clouds (Yusef-Zadeh et al. 1999). The velocity and velocity gradients seen in the OH masers,  $\sim 2 \text{ km s}^{-1} \text{ pc}^{-1}$ , are similar to those observed in the  $50 \text{ km s}^{-1}$  cloud. Yusef-Zadeh et al. (1999) argue that the OH masers arise from the interaction of Sgr A East with the  $50 \text{ km s}^{-1}$  cloud which is located within 5 pc behind the Galactic center. Absorption of the continuum radiation from Sgr A East by Sgr A West at cm wavelengths (Yusef-Zadeh & Morris 1987; Pedlar et al. 1989), locates Sgr A East behind Sgr A West. The red and blue-shifted gas  $100''$  to the east suggest that the  $50 \text{ km s}^{-1}$  cloud and Sgr A East are at about the same distance. Position-velocity cut 'f' in Figure 13 traces gas in the northern part of the  $50 \text{ km s}^{-1}$  cloud, where it wraps around the expanding shell of Sgr A East. Emission in the upper half of the figure is red-shifted to  $+60$  to  $+80 \text{ km s}^{-1}$  and has a narrower linewidth than the gas near the core of the GMC, seen in the lower half of the diagram from  $-20$  to  $-80 \text{ arcsec}$ . We do not see corresponding blue-shifted emission in the northern part, which implies that this gas must be located *behind* and adjacent to Sgr A East.

Figure 16 shows a progression to the east of the Galactic Center of high-velocity HCN(1-0) and  $\text{HCO}^+$ , followed by the ridge of  $\text{NH}_3$ , and a string of HII regions. The high-velocity gas is accelerated and shocked by Sgr A East, which may be comprised of several expanding supernova shells. The HII regions are at a larger radius than the the current wave of compressed gas, and must trace an earlier epoch of star formation.

### 5.5. Comparison to $\text{NH}_3$

The  $\text{NH}_3(1,1)$  and (2,2) distributions are very similar (Coil & Ho 1999, 2000), as are the  $\text{HCO}^+$  and HCN(1-0). The comparable angular resolution and spatial coverage of these data sets makes a comparison of  $\text{NH}_3$  to HCN and  $\text{HCO}^+$  results of immediate interest. However, the velocity range and spatial coverage of the  $\text{NH}_3(1,1)$  data do not match that of the HCN(1-0) data. HCN(1-0) and  $\text{HCO}^+$  were observed over the velocity range  $-150$  to  $+150 \text{ km s}^{-1}$  in a mosaic pattern covering the central  $5'$ . The VLA observations of  $\text{NH}_3(1,1)$  and (2,2) were obtained in 5 fields. The central and northern field cover  $-75$  to  $+55 \text{ km s}^{-1}$ ; the southern and two eastern fields cover  $-40$  to  $+90 \text{ km s}^{-1}$ . Figure 14 plots HCN(1-0) and  $\text{NH}_3(1,1)$  emission in six velocity ranges covering the total velocity interval of  $-75 \text{ km s}^{-1}$  to  $+90 \text{ km s}^{-1}$ . The single outer contour shows the spatial extent of the mosaic primary beam pattern for the  $\text{NH}_3(1,1)$  data in each velocity range.

The  $\text{NH}_3$  emission is brightest in two parallel ridges running from the northeast to southwest across the mosaic in the velocity range of  $0$  to  $60 \text{ km s}^{-1}$  as seen in Coil & Ho (2000). Figure 14 shows patchy HCN(1-0) emission in this region, but these ridges are not as apparent in HCN as in  $\text{NH}_3$ . Another difference between the HCN and  $\text{NH}_3$  emission is that the  $\text{NH}_3$  does not trace the high-velocity features seen in the CND in HCN(1-0). This is most noticeable in the top left and bottom right panels where the HCN shows strong emission from the CND while there is no

indication of  $\text{NH}_3$  emission at these velocities. Figure 15 compares the spectra of HCN(1-0) and  $\text{NH}_3(1,1)$  at the positions of the  $\text{NH}_3(1,1)$  peaks from Coil & Ho (2000). The  $\text{NH}_3(1,1)$  spectra have been scaled and shifted to match the height of the HCN line and are shown for comparison of the line shape only and not the absolute flux level. In most of these spectra, a deep absorption feature is seen in HCN(1-0) at the position of the peak  $\text{NH}_3(1,1)$  emission.

#### *Effects in the GMCs*

The high abundance and high optical depths of HCN(1-0) and  $\text{HCO}^+(1-0)$  make these tracers particularly susceptible to absorption along the line of sight as compared to  $\text{NH}_3$ . Gas along the line of sight that is not related to the Galactic center and is at a lower column density and temperature may cause absorption. This can occur either because of a lower physical temperature or a lower volume density leading to a lower excitation temperature. In examining the spectra in Figure 9, it is clear that most of the narrow absorption dips are due to intervening matter which are not located at the Galactic Center. These dips are not seen in the higher transitions of HCN (Marshall, Lasenby, & Harris 1995) which suggests that the absorbing material is probably cold and at a low enough density that the upper levels are not populated. The absence of the dips in  $\text{NH}_3$  is probably due to its relatively lower abundance and hence lower optical depths. However, even in  $\text{NH}_3$ , absorption can be seen in deep integrations (Serabyn & Güsten 1986).

The high optical depth of the HCN(1-0) and  $\text{HCO}^+$  lines can also lead to self-absorption by cool outer layers of a cloud. This self-absorption may account for the lack of HCN(1-0) and  $\text{HCO}^+$  emission from the more massive GMCs. Position-velocity cuts *a* and *b* (Figure 8) run along the ridges seen in  $\text{NH}_3(1,1)$  and (2,2) emission. The double-peaked profiles seen in Figure 13 from  $0$  to  $60 \text{ km s}^{-1}$  indicate that the HCN(1-0) emission is self-absorbed along the ridges of  $\text{NH}_3$  emission. Self-absorption to the south of the CND can also be seen in position-velocity cuts *c* and *d*. Cut *f* shows additional self-absorption to the northeast in the region of the  $50 \text{ km s}^{-1}$  cloud core (but not in the northern part of the ridge, where the gas is red-shifted). The location of the  $\text{NH}_3$  emission in the absorption dips of the HCN(1-0) emission (Figure 15) is a signature of self-absorption in the HCN(1-0). The HCN and  $\text{HCO}^+$  spectra are highly correlated with each other, and the  $\text{HCO}^+$  is also highly self-absorbed.

From the strength of the dips due to line of sight absorption and self-absorption we estimate that absorption by intervening material may lead to underestimates of HCN emission by a factor of  $\sim 2$ , while self-absorption by the outer parts of clouds can have a stronger effect of up to a factor of  $\sim 5$  underestimation of the emission.

#### *Effects in the CND*

Position velocity cut *b* also shows emission from the CND from  $-100 \text{ km s}^{-1}$  at a position of  $-20''$  to  $+120 \text{ km s}^{-1}$  at a position of  $+100''$ . This emission does not appear to be self-absorbed which implies that the optical depth is lower in the CND than in the GMCs. The high optical depth of HCN(1-0) in the Galactic Center may explain why it is brightest in the CND. Gas in the CND typically has very broad ( $\geq 50 \text{ km s}^{-1}$ ) line widths. For a very optically thick line, the line wings will also be optically

thick and the broadened line will appear brighter in total flux than an optically thick but narrow line. However, for an optically thin tracer, the broadening in the CND will only make the line weaker as the emission that was originally confined to a narrow velocity range is spread out into a broad line. In that case, the total flux remains the same. Although opacity may not account entirely for the differences in HCN(1-0) and NH<sub>3</sub> emission, it is clear that HCN images will preferentially show line broadened emission from the CND while emission from the GMCs will be relatively weaker due to both the narrow line width and self-absorption.

The differences in the NH<sub>3</sub> and HCN maps may also be due to a variety of chemistry and temperature effects in the region. Using a large velocity gradient (LVG) model, Marshall, Lasenby, & Harris (1995) derive an HCN abundance of  $\sim 10^{-9}$  with a molecular density  $n[\text{H}_2] \sim 10^6 \text{ cm}^{-3}$  from a comparison of HCN(4-3) and (3-2) emission in the CND, consistent with normal abundances. However, the analysis of just two transitions which may be optically thick is not very sensitive to abundance enhancement. From a comparison of HCN J=1-0, H<sup>13</sup>CN J=1-0, and HCN J=3-2 (Jackson et al. 1993), Marr, Wright, & Backer (1993) derive an HCN J=1-0 opacity of 2-4 in the CND, with  $T_{\text{gas}} \sim 250\text{K}$  and  $n[\text{H}_2] \sim 10^6 \text{ cm}^{-3}$ . The derived abundances of HCN and HCO<sup>+</sup> are  $\sim 8 \cdot 10^{-8}$  and  $\sim 10^{-9}$  which are enhanced by at least an order of magnitude over typical values. This abundance enhancement could also account for the relative brightness of the CND in HCN and HCO<sup>+</sup> compared to other tracers.

NH<sub>3</sub> does not appear to be greatly enhanced in the southern streamer where Coil & Ho (1999) found that the brightness of the NH<sub>3</sub> was consistent with a “typical” abundance of  $\text{NH}_3/\text{H}_2 \approx 10^{-8}$ . The relative weakness of NH<sub>3</sub> emission from the CND may also indicate that the NH<sub>3</sub> is underabundant in the ring in addition to the opacity effects discussed above. The small amount of NH<sub>3</sub> emission that does appear to come from the CND is found in low-ionization regions on the outer edge of the CND, with modest temperatures of 60–70 K (Coil & Ho 2000). This result matches the dust temperature of 76 K at a radius of about 50'' (Latvakoski et al. 1999). These cooler regions of the CND are shielded from UV photons which could destroy the NH<sub>3</sub> molecule. While NH<sub>3</sub>, HCN and HCO<sup>+</sup> are all dissociated by ionizing radiation from the center, HCN and HCO<sup>+</sup> may be more efficiently reformed than NH<sub>3</sub> in the post-shock chemistry as a result of cloud-cloud collisions in the CND. This could enable the abundances of HCN and HCO<sup>+</sup> to remain high in the CND. If the CND is comprised of infalling gas on parabolic orbits, the infall time from a radius of 1.4 pc at a velocity 140 km sec<sup>-1</sup> is  $\sim 10^4$  yrs. Models of the chemical evolution for the Orion Hot Core (e.g. (Charnley, Tielens & Millar 1992)), predict a decreased NH<sub>3</sub> abundance and an enhanced HCN abundance after  $\sim 10^4$  yrs in an environment similar to the CND at 1 pc radius. The grain mantles may be completely removed by this time and the gas phase NH<sub>3</sub>, no longer replenished by mantle evaporation, is destroyed by UV photons in the inner CND environment.

### 5.6. Comparison with 1.2mm Dust

Figure 17 shows contours of velocity-integrated HCN and NH<sub>3</sub> emission overlaid on an image of the continuum emission at 1.2 mm (Zylka 1998). The center of the 1.2 mm image is dominated by free-free and dust emission associated with ionized gas in Sgr A West. Outside the center, the 1.2 mm image traces emission from dust with column density  $3\text{-}8 \times 10^{23} \text{ cm}^{-2}$ . The two ridges of NH<sub>3</sub> emission agree well with the dust emission indicating that dust and NH<sub>3</sub> are related. The HCN and HCO<sup>+</sup> emission agree well with the dust emission when the effects of self-absorption are considered.

The eastern ridge of NH<sub>3</sub> (1,1) emission is coincident with the eastern edge of Sgr A East where it is impacting the 50 km s<sup>-1</sup> cloud. In addition, a supernova shell to the south of Sgr A East was suggested by Coil & Ho (2000), centered at  $\sim \Delta_{RA} = 80'', \Delta_{DEC} = -120''$ . The shell can be seen as wispy 6cm emission which seems to impact the southern side of Sgr A East (see Figure 16). The western edge of this shell is coincident with the “southern streamer” seen in NH<sub>3</sub> emission. A string of OH masers (A, E, D, G1) coincides with the bright middle clump of the “southern streamer.” NH<sub>3</sub> emission is seen outside these regions, so shock excitation probably does not account for all of the observed NH<sub>3</sub> emission. However, NH<sub>3</sub> emission in the molecular ridge and “southern streamer” may be enhanced in locations where expanding shells are pushing into dense molecular gas.

A possible explanation of the correlation between NH<sub>3</sub> and dust emission and the location of shocks is that the NH<sub>3</sub> lies on the edge of GMCs where shocks are heating the grain mantles. In a dynamical model of nitrogen molecules in molecular clouds Nejad et al. (1990) found that NH<sub>3</sub> may be formed and stored on grains and subsequently released in shocks thus providing the gas phase NH<sub>3</sub>. In this thin outer layer of the cloud, the grains release NH<sub>3</sub> as they are heated and disrupted, thus enhancing the abundance of NH<sub>3</sub>. The NH<sub>3</sub> will be warmer than the unperturbed dust in the interior portions of the cloud, therefore giving a higher excitation temperature than the dust. This scenario requires that the layer of enhanced NH<sub>3</sub> abundance is thin so that the total brightness of NH<sub>3</sub> is consistent with an abundance of  $10^{-8}$  averaged throughout the entire cloud (Coil & Ho 1999, 2000). It should also be noted that Terzieva & Herbst (2000) found that the observed abundances of NH<sub>3</sub> can be produced using only ion-molecule chemistry. Thus the extent to which the dust grains play a role cannot be determined.

Unfortunately, the present data do not enable us to distinguish between the theories proposed above. It is possible that all of these effects have roles of various importance in the region.

## 6. CONCLUSIONS

i) We present images of HCN(1-0) and HCO<sup>+</sup> emission and absorption which trace dense molecular gas in the central 12 parsecs of the Galaxy. The HCN(1-0) and HCO<sup>+</sup> emission primarily traces filamentary structures associated with the CND and nearby GMCs; low-level, extended emission from partially-resolved larger structures is also seen.

ii) The CND appears as a bright, well-defined ring of emission 20''–60'' from the center, at an inclination of 60–

70°. Although the outer edge of the ring is not as sharply defined as the inner edge, the CND does not extend beyond 100'' in HCN(1-0) and HCO<sup>+</sup> emission. The CND does not appear to be an equilibrium structure; rather, it consists of two or three separate streamers in rotation around the nucleus. The CND may exist long-term in a fluctuating sense, as gas streamers feed the inner parsec.

iii) Outside the CND, HCN(1-0) and HCO<sup>+</sup> trace several filamentary structures which do not follow the rotation pattern of the 45'' ring. High-velocity emission is seen 90'' east of Sgr A\*, just inside the dense molecular ridge of shocked material seen at the intersection of Sgr A East and the 50 km sec<sup>-1</sup> cloud. A stream of emission is also seen extending from the ionized northern arm, through the CND to high-velocity red- and blue-shifted material to the north. This material may be falling into the center on an orbit which intersects the CND streamers.

iv) Comparison of the HCN(1-0) and HCO<sup>+</sup> with NH<sub>3</sub> and dust emission shows that NH<sub>3</sub> emission is well correlated with self-absorbed HCN(1-0) and HCO<sup>+</sup> emission, and dust ridges in the nearby GMCs.

v) HCN(1-0) and HCO<sup>+</sup> emission appear to be enhanced in the CND relative to NH<sub>3</sub>. Further observations of other spectral lines are required to distinguish between opacity, excitation and chemical explanations for these differences.

These observations show that the accretion of material into the Galactic Center region may be a chaotic and transient phenomenon. From the spatial distribution of the nearby gas with respect to Sgr A East and other nearby supernova remnants, and from the overall kinematics and especially the isolated pockets of high-velocity gas, we have the impression that the nearby molecular clouds are being disrupted by the expanding shells associated with Sgr A East. Infall of material appears to approach the CND from a number of different directions on different orbits. Sgr A East itself may be driven by multiple outflow events associated with the central black hole or multiple supernovae. We favor a model where the accretion process is highly non-steady and non-uniform at least on the timescale of the rotation period of the CND, 10<sup>5</sup> yrs. In this scenario, the CND does not appear uniform because material continues to fall into the CND on short timescales. Whether the further infall of material from the CND toward the central black hole is also transient and non-steady in nature is unclear from these studies. However, there is some evidence that material may approach the central region directly from outside of the CND via individual streamers.

*Acknowledgments* This work was supported in part by NSF Grant AST-21795 to the University of California. ALC is supported by an NSF Graduate Research Fellowship. We thank Robert Zylka for permission to use the 1.2 mm image.



## REFERENCES

- Charnley, S.B., Tielens, A.G.G.M., & Millar, T.J. 1992, *ApJ*, 399, L71
- Coil, A.L. & Ho, P.T.P. 1999, *ApJ*, 513, 752
- Coil, A.L. & Ho, P.T.P. 2000, *ApJ*, 533, 245
- Davies, C.J. & Dent, W.R.F. 1993, *MNRAS*, 261, 371
- Dent, W. R. F., Matthews, H. E., Wade, R. & Duncan, W. D. 1993, *ApJ*, 410, 650
- Ekers, R. D., van Gorkom, J. H., Schwarz, U. J. & Goss, W. M. 1983, *A&A*, 122, 143
- Frail, D.A., Diamond, P.J., Cordes, J.M. & van Langevelde, H.J. 1994, *ApJ*, 427, 43
- Gatley, I., Beattie, D.H., Lee, T.J., Jones, T.J. & Hyland, A.R. 1984, *MNRAS*, 210, 565
- Genzel, R., Watson, D. M., Crawford, M. K. & Townes, C. H. 1985, *ApJ*, 297, 766
- Genzel, R., Stacey, G. J., Harris, A. I., Geis, N., Graf, U. U., Poglitsch, A. & Sutzki, J. 1990, *ApJ*, 356, 160
- Genzel, R., Eckart, A., Ott, T. & Eisenhauer, F. 1997, *MNRAS*, 291, 219
- Ghez, A. M., Klein, B. L., Morris, M. & Becklin, E. E. 1998, *ApJ*, 509, 678
- Goss, W. M., Schwarz, U. J., van Gorkom, J. H. & Ekers, R. D. 1985, *MNRAS*, 215, 69
- Güsten, R. & Downes, D. 1981, *A&A*, 99, 27
- Güsten, R., Genzel, R., Wright, M. C. H., Jaffe, D. T., Stutzki, J. & Harris, A. I. 1987, *ApJ*, 318, 124
- Güsten, R., Walmsley, C. M. & Pauls, T. 1981, *A&A*, 103, 197
- Ho, P.T.P., Jackson, J.M., Barrett, A.H. & Armstrong, J.T. 1985, *ApJ*, 288, 575
- Ho, P. T. P., Ho, L. C., Szczepanski, J. C., Jackson, J. M., Armstrong, J. T. & Barrett, A. H. 1991, *Nature*, 350, 309
- Ho, P.T.P. 1993, *Proc. IAU Colloquium No.140*
- Jackson, J. M., Geis, N., Genzel, R., Harris, A. I., Madden, S., Poglitsch, A., Stacey, G. J. & Townes, C. H. 1993, *ApJ*, 402, 173
- Lacy, J. H., Achtermann, J. M. & Serabyn, E. 1991, *ApJ*, 380, 71
- Latvakoski, H. M., Stacy, G. J., Gull, G. E., & Hatward, T. L. 1999, *ApJ*, 511, 761
- Lo, K. Y. & Claussen, M. J. 1983, *Nature*, 306, 647
- Lugten, J. B., Genzel, R., Crawford, M. K., & Townes, C. H. 1986, *ApJ*, 306, 691
- Marr, J. M., Wright, M. C. H. & Backer, D. C. 1993, *ApJ*, 411, 667
- Marshall, J., Lasenby, A. N. & Harris, A. I. 1995, *MNRAS*, 277, 594
- Mezger, P.G., Zylka, R., Salter, C.J., Wink, J.E., Chini, R., Kreyesa, E., & Tuffs, R., 1989, *A&A* 209, 337
- Morris, M. & Serabyn, E. 1996, *ARA&A*, 34, 645
- Morris, M., Zuckerman, B., Palmer, P., & Turner, B. E., 1973, 186, 501
- Nejad, L.A.M., Williams, D.A. & Charnley, S.B. 1990, *MNRAS*, 246, 183
- Okumura, S. K., Ishiguro, M., Fomalont, E. B., Chikada, Y., Kasuga, T., Morita, K., Kawabe, R., Kobayashi, H., Kanzawa, T., Iwashita, H. & Hasegawa, T. 1989, *ApJ*, 347, 240
- Pedlar, A., Anantharamaiah, K., R., Ekers, R., D., Goss, W.M., van Gorkom, J., H., Schwartz, U., J., & Zhao, J.-H. 1989, *ApJ*, 342, 769
- Roberts, D.A. & Goss, W.M. 1993, *ApJS*, 86, 133
- Sandford, S.A. & Allamandola, L.J. 1993, *ApJ*, 417, 815
- Sault, R.J., Teuben, P.J. & Wright, M.C.H. 1995, *A Retrospective View of Miriad, in: Astronomical Data Analysis Software and Systems IV*, ed. R.A. Shaw, H.E. Payne & J.J.E. Hayes. *PASP Conf Series* 77, 433 (1995)
- Sault, R.J., Staveley-Smith, L. & Brouw, W.N. 1996, *A&A Supp.*, 120, 375
- Serabyn, E., Lacy, J. H. & Achtermann, J. M. 1992, *ApJ*, 395, 166
- Serabyn, E. & Güsten, R. 1986, *A&A*, 161, 334
- Steer, D.G., Dewdney, P.E. & Ito, M.R. 1984, *A&A*, 137, 159
- Sutton, E.C., Danchi, W.C., Jaminet, P.A. & Masson, C.R., 1990, *ApJ*, 348, 503
- Terzieva, R., & Herbst, E., 2000, *ApJ*, 501, 207
- Tsuboi, M., Handa, T., & Utika, N., 1999, *ApJ* *supp* 120, 1
- Wardle, M., Yusef-Zadeh, F. & Geballe, T.R. 1998 in: "The Central Parsecs of the Galaxy", *A.S.P. Conf. SER.* 186, H. Falcke (ed.), p. 432
- Welch, W. J. Thornton, D. D. Plambeck, R.L., Wright, M.C.H., Lugten, J., Urry, L., Fleming, M., Hoffman, W., Hudson, J., Lum, W.T., Forster, J.R., Thatte, N., Zhang, X., Zivanovic, S., Snyder, L., Crutcher, R., Lo, K.Y., Wakker, B., Stupar, M., Sault, R., Miao, Y., Rao, R., Wan, K., Dickel, H., R., Blitz, L., Vogel, S.N., Mundy, L., Erickson, W., Teuben, P.J., Morgan, J., Helfer, T., Looney, L., de Gues, E., Grossman, A., Howe, J.E., Pound, M. & Regan, R. 1996, *PASP*, 108, 93
- Wright, M.C.H. 1999, "Image Fidelity", *BIMA memo* 73, <http://bima.astro.umd.edu/memo/memo.html>, *BIMA memo* 73
- Wright, M.C.H. & Backer D.C. 1993, *ApJ*, 417, 560
- Yusef-Zadeh, F. & Morris, M. 1987, *ApJ*, 320, 545
- Yusef-Zadeh, F., Roberts, D. A., Goss, W. M., Frail, D. A., & Green, A. J. 1999, *ApJ*, 512, 230
- Zylka, R. 1998, *IAU Symp.* 184, *The Central Regions of the Galaxy and Galaxies*, ed. Y. Sofue (Dordrecht:Kluwer), 156
- Zylka, R., Mezger, P.G., & Wink, J., E., 1990, *A&A* 234, 133

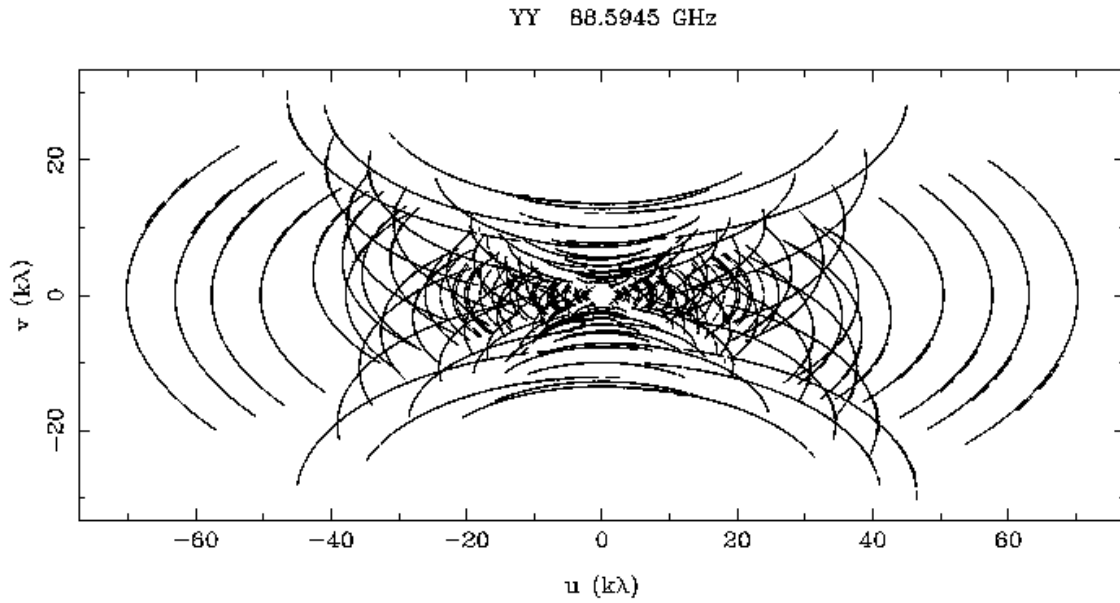


FIG. 1.—  $uv$  coverage of our BIMA observations.

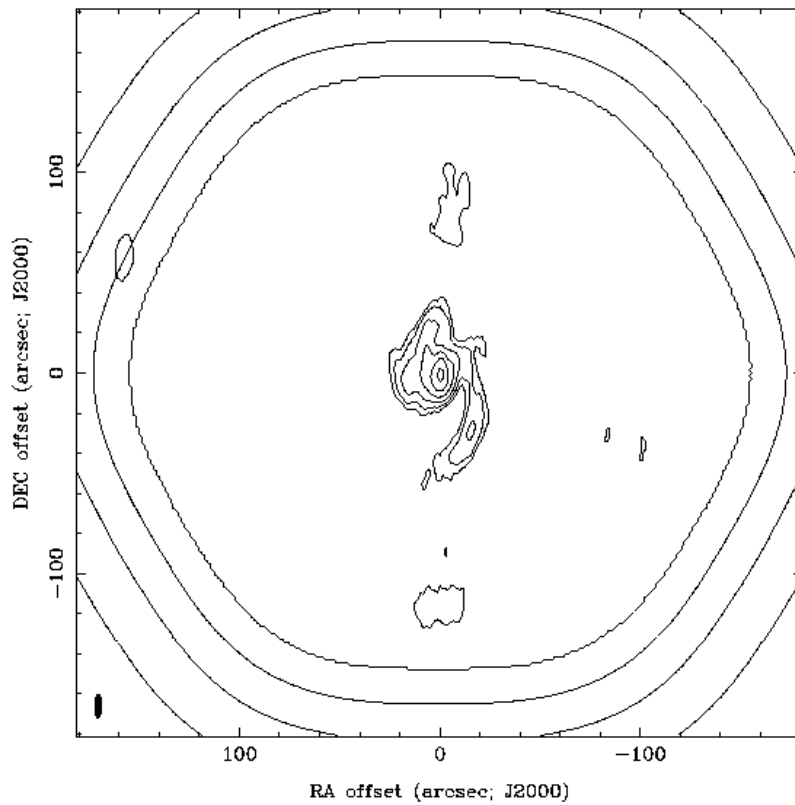


FIG. 2.— Continuum emission at contour levels .05, .1, .2, .4, .8, 1.6  $\text{Jy beam}^{-1}$ . The synthesised beam FWHM is shown in the bottom left corner. The effective primary beam attenuation in the mosaic image is indicated at levels 0.25, 0.5, 0.75, 1.0.

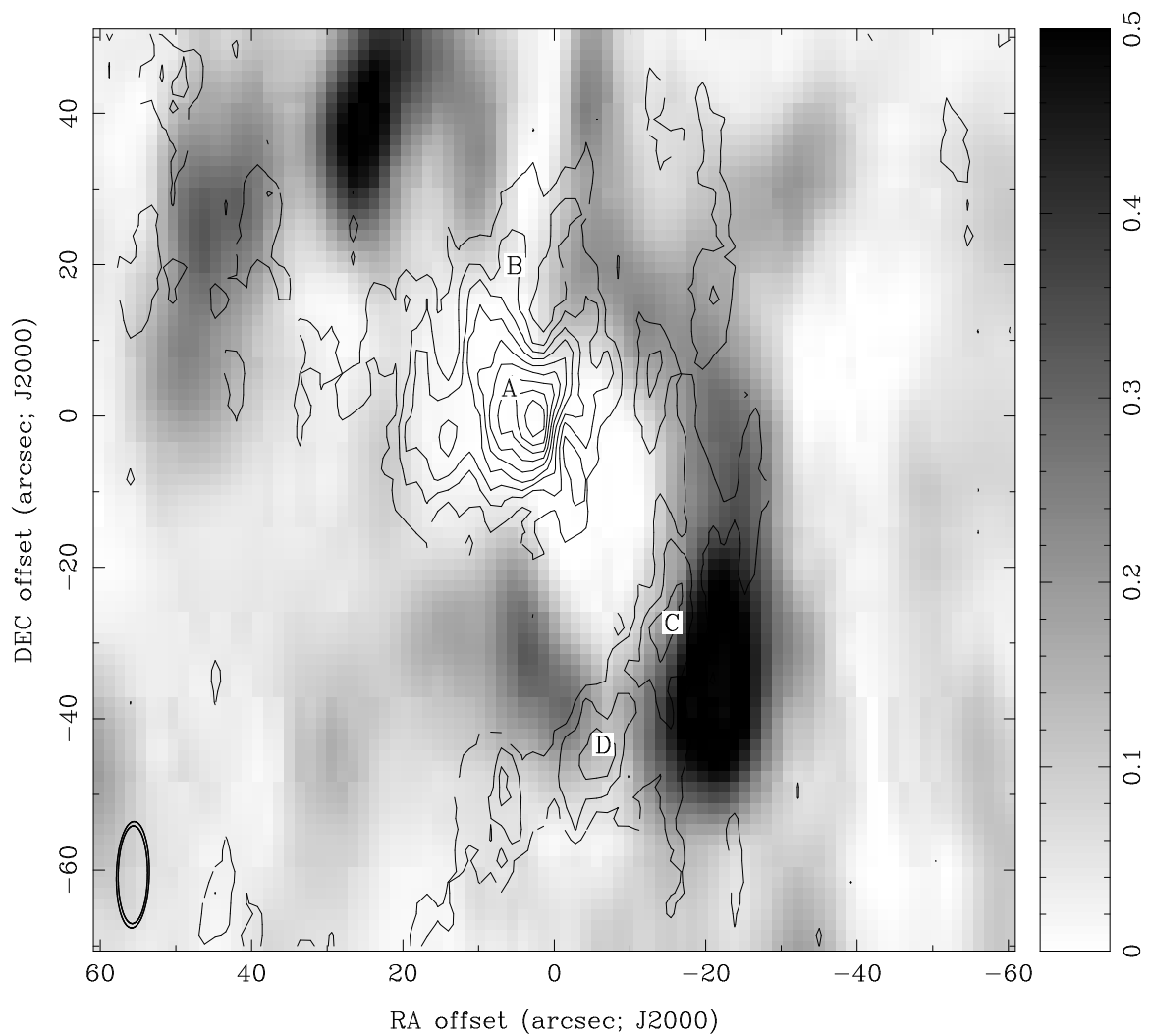


FIG. 3.— H  $42\alpha$  emission integrated from  $-150$  to  $+150$   $\text{km s}^{-1}$ . Contours are at intervals of  $12.5$   $\text{mJy beam}^{-1}$  from  $12.5$  to  $125$   $\text{mJy beam}^{-1}$ . The grey scale image is the HCN(1-0) emission integrated from  $-150$  to  $+150$   $\text{km s}^{-1}$ . The positions of H  $42\alpha$  spectra are indicated. The synthesised beam FWHM is shown in the bottom left corner. The position of OH maser B from Yusef-Zadeh et al. (1999) is marked by an “X”.

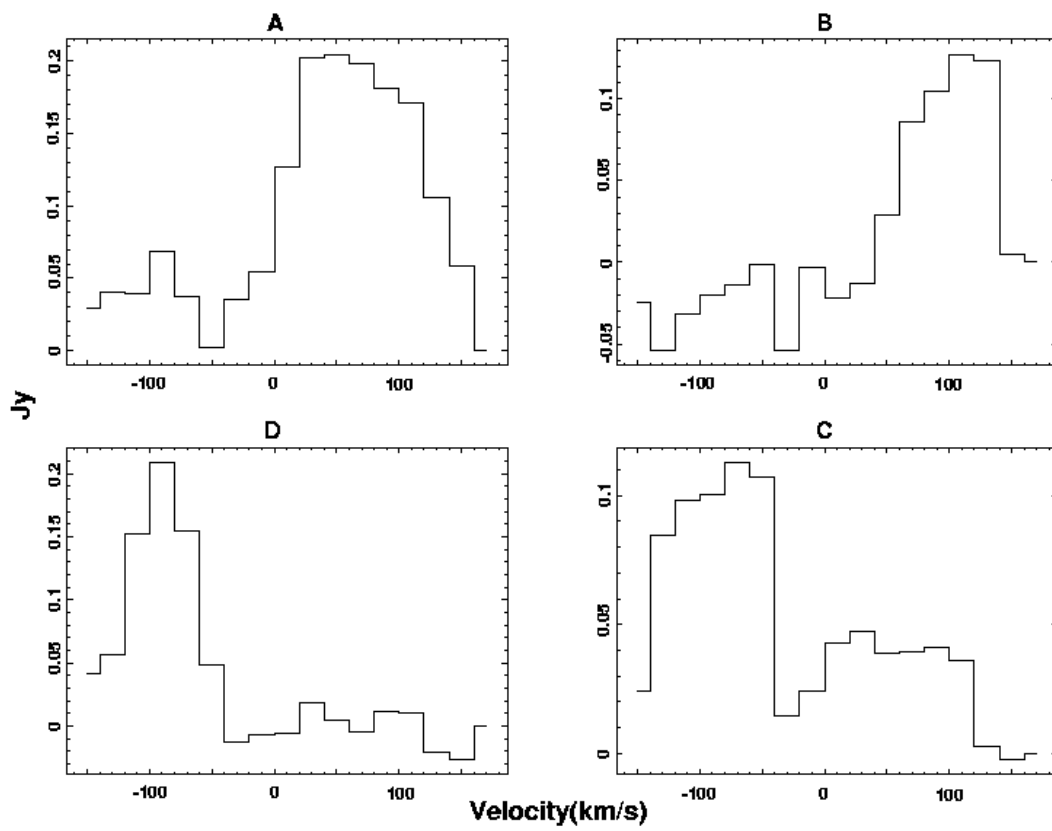


FIG. 4.— H 42 $\alpha$  spectra at positions marked in Figure 3.

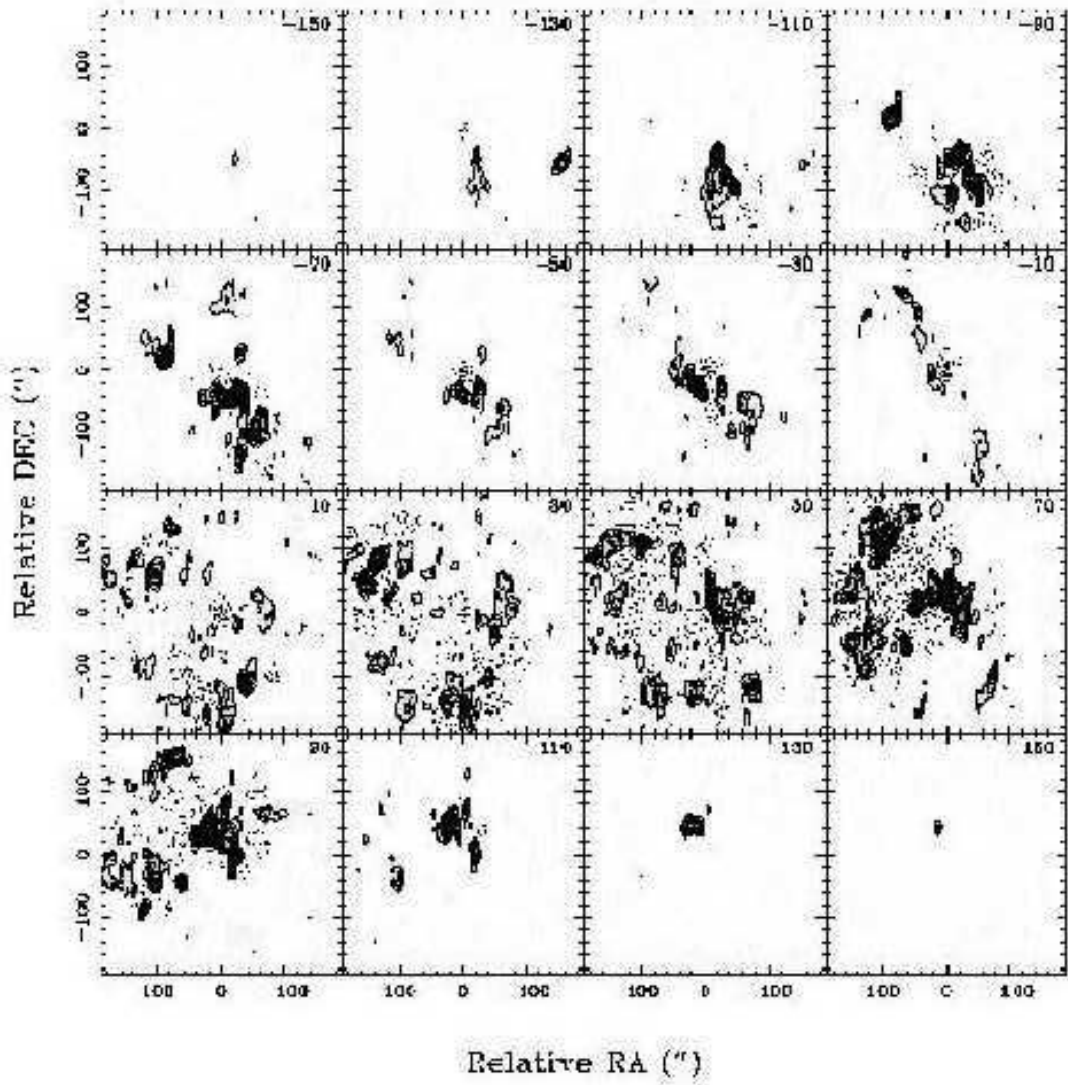


FIG. 5.— Images of HCN(1-0) emission in  $20 \text{ km s}^{-1}$  intervals. The contour interval is  $0.25 \text{ Jy beam}^{-1}$  ( $0.6 \text{ K}$ ).

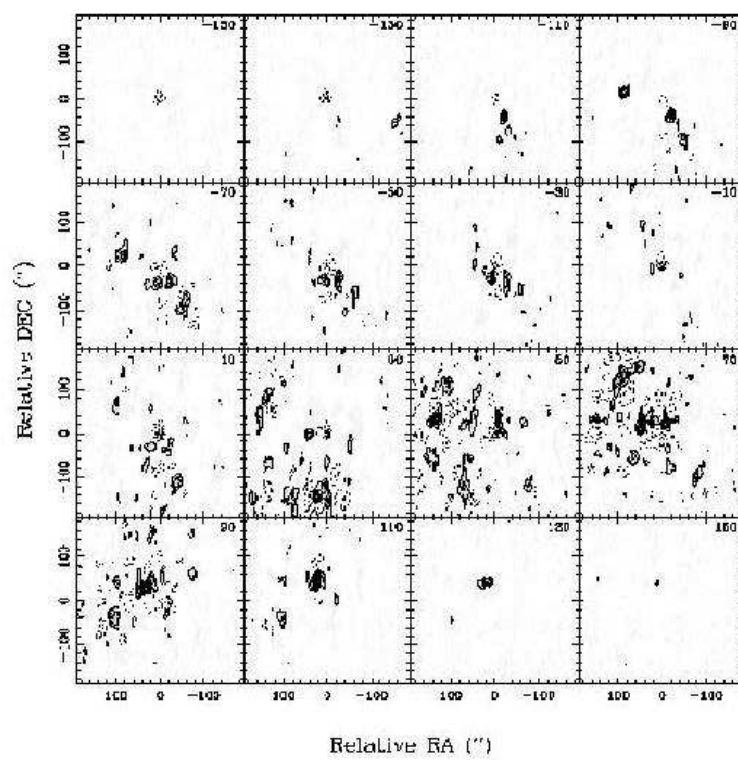


FIG. 6.— Images of  $\text{HCO}^+$  emission in  $20 \text{ km s}^{-1}$  intervals. The contour interval is  $0.25 \text{ Jy beam}^{-1}$  ( $0.6 \text{ K}$ ).

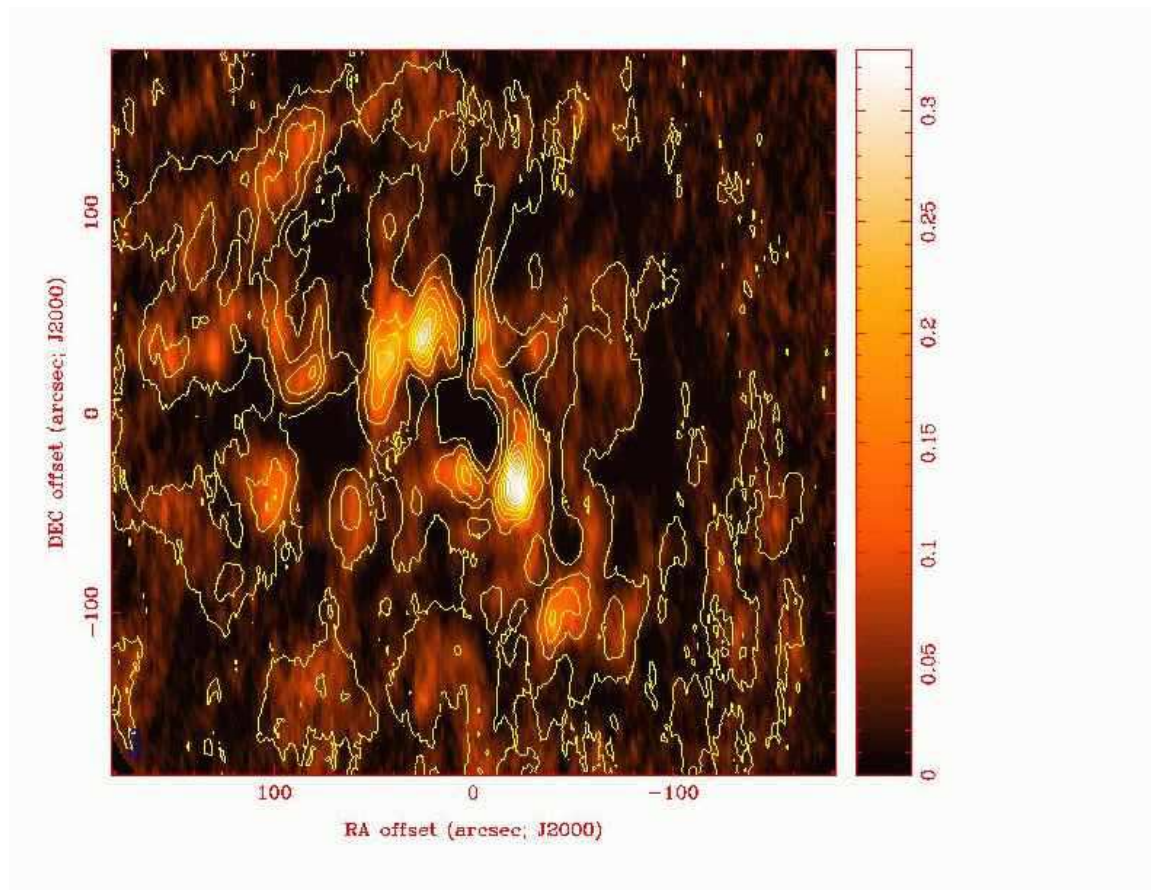


FIG. 7.— Comparison of HCN(1-0) (contours) and HCO<sup>+</sup> (grey/color image) emission. Contours from 0.04 to 0.78 Jy beam<sup>-1</sup>. (3.5 K/Jy)

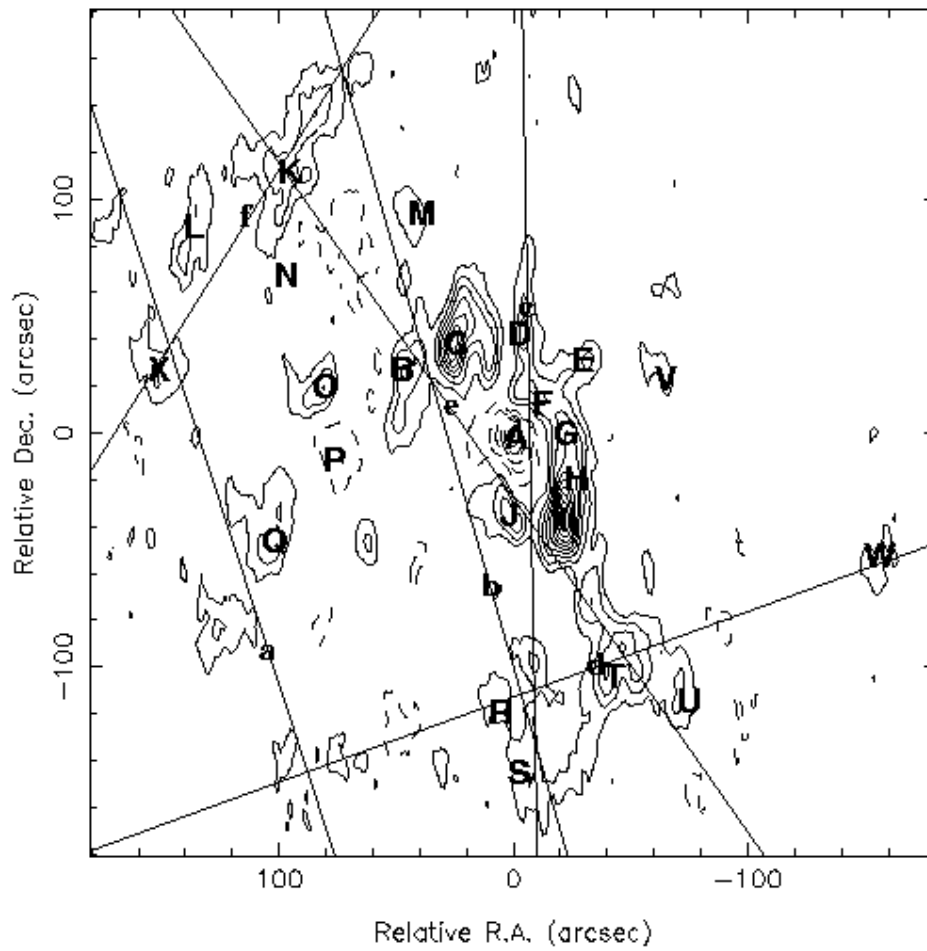


FIG. 8.— HCN(1-0) and  $\text{HCO}^+$  spectra positions (labeled A to X) and position-velocity cuts along lines (labeled a to f), superposed on contours of HCN emission integrated from  $-150$  to  $150 \text{ km s}^{-1}$ . The contour interval is  $0.213 \text{ K}$ .



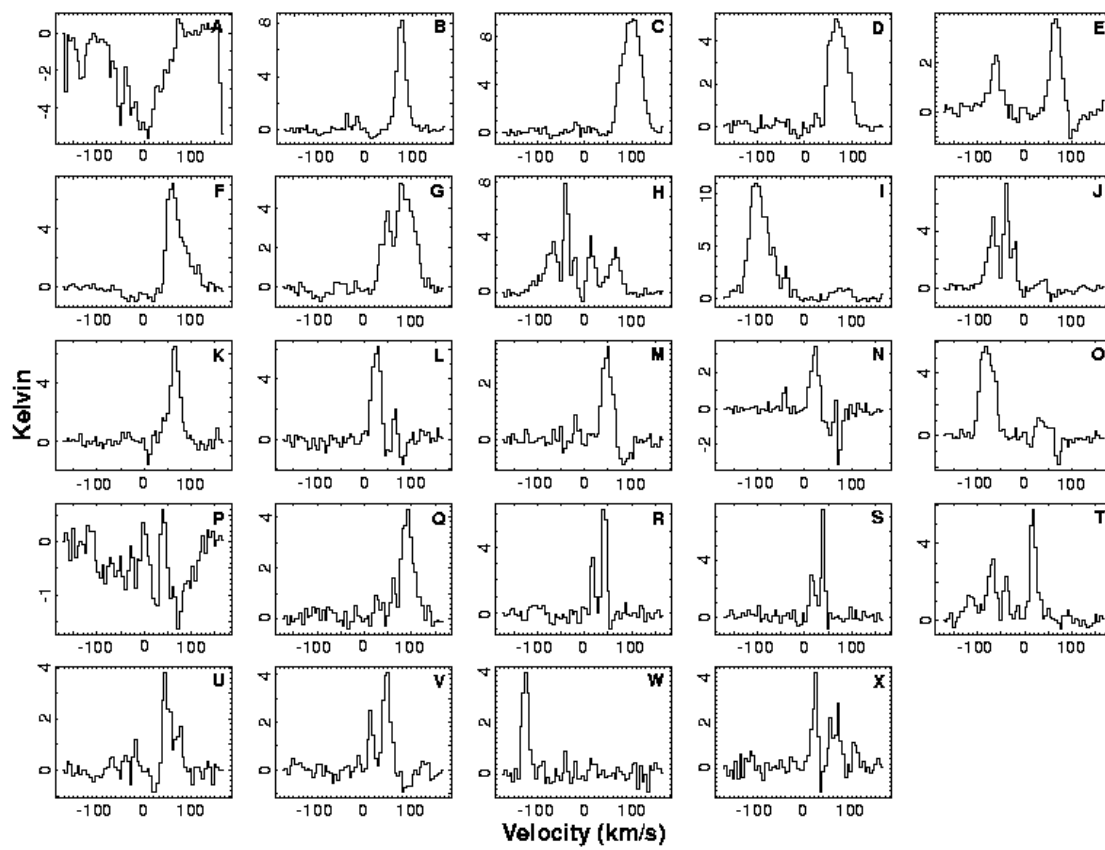


FIG. 9.— HCN(1-0) spectra at positions shown Figure 8.

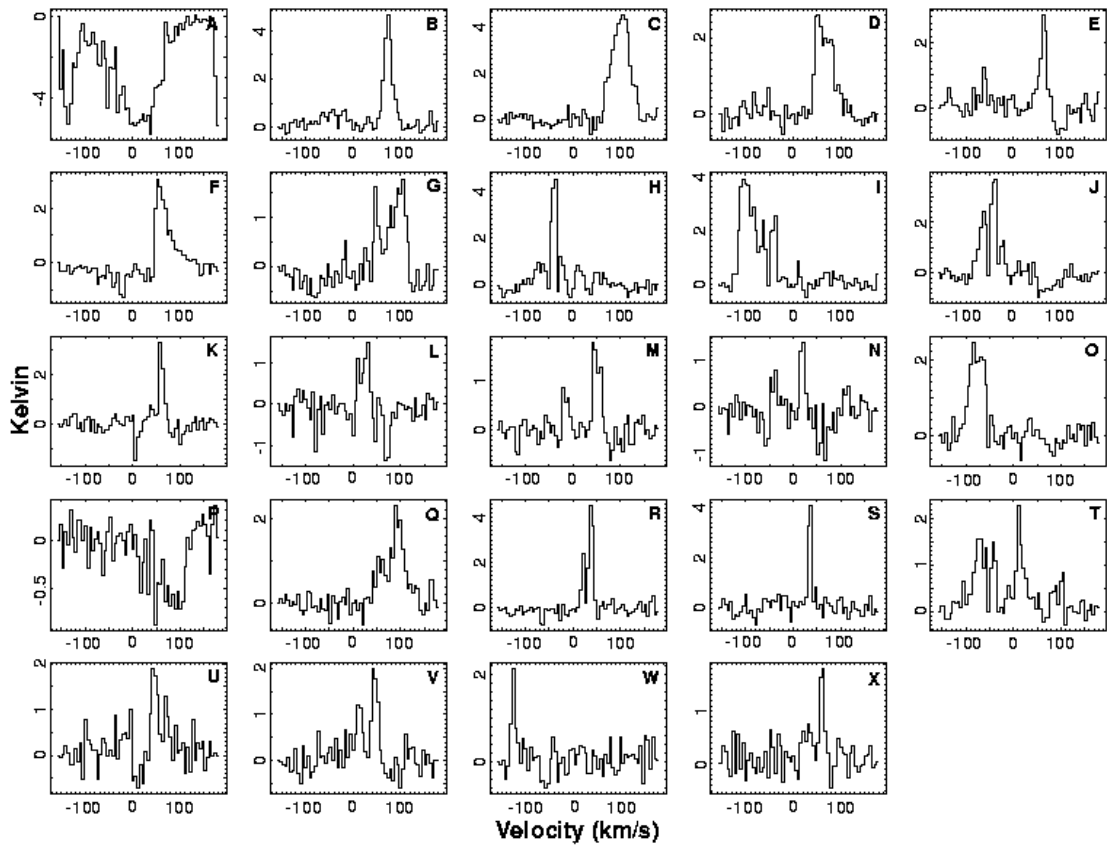


FIG. 10.— HCO<sup>+</sup> spectra at positions shown Figure 8.

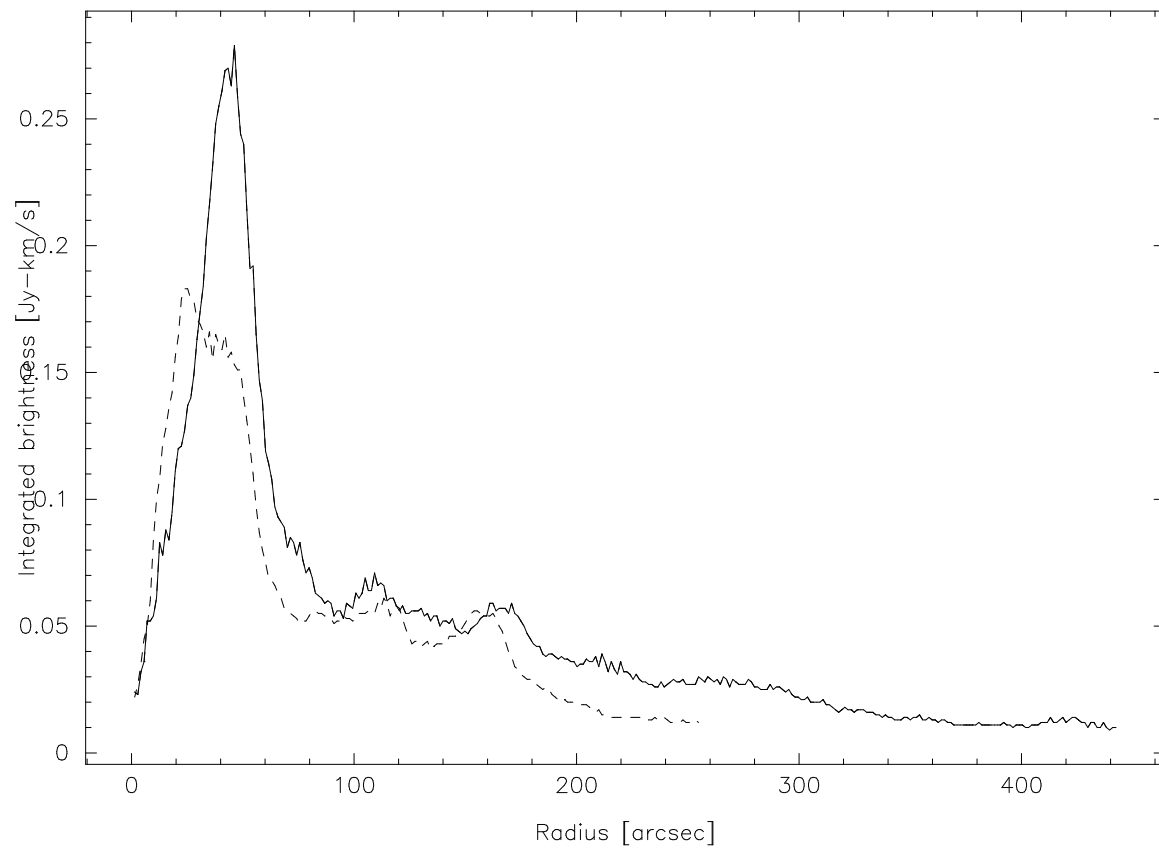


FIG. 11.— Radial profile of HCN(1-0) emission averaged around elliptical annuli. As it is not clear whether the more extended emission is in the same plane as the CND (which itself may not lie in one plane), figure 11 shows radial profiles in the plane of the sky (dashed line), and de-projected from an inclination of  $56^\circ$  (solid line).

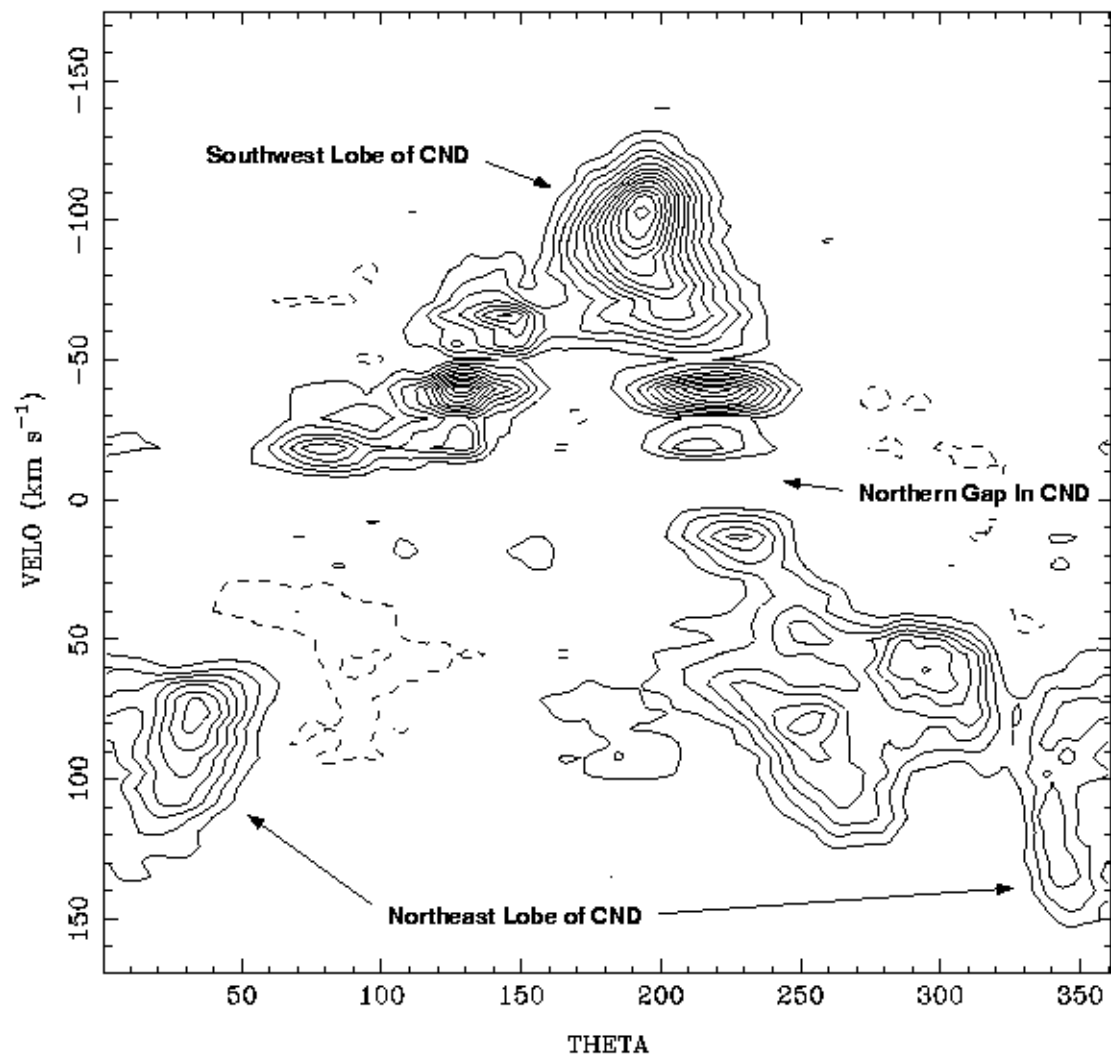


FIG. 12.— Position-velocity diagram of emission in the CND.

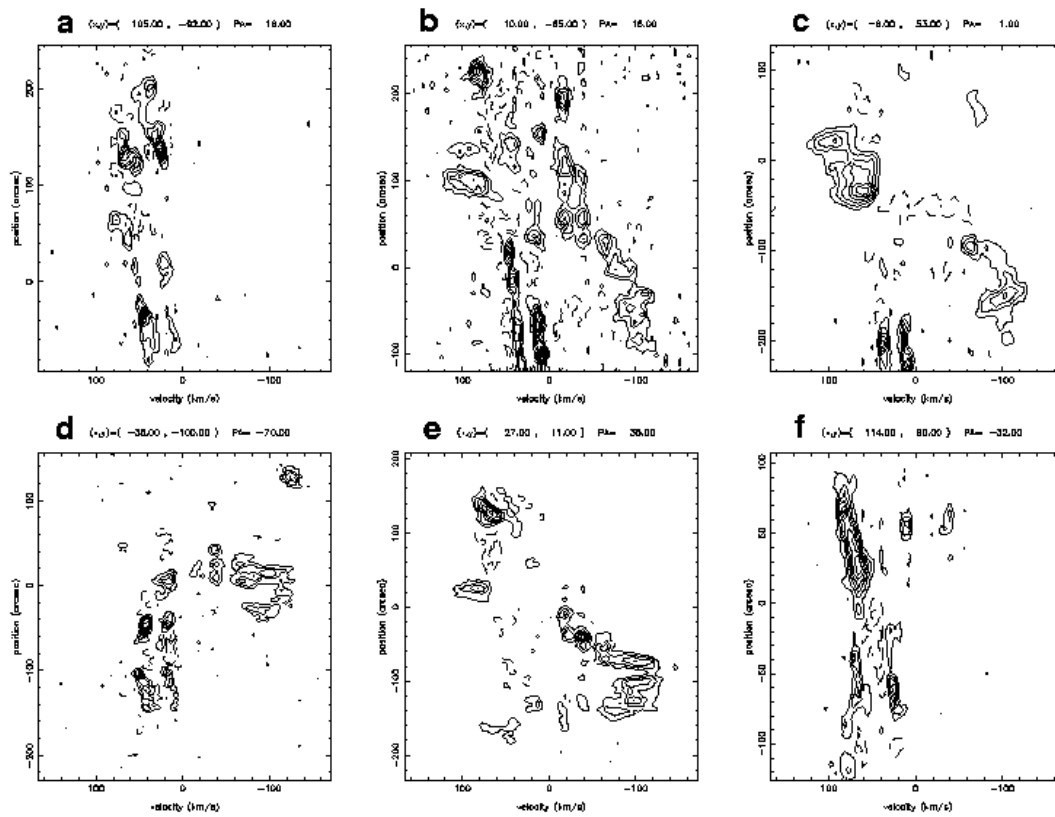


FIG. 13.— Position velocity cuts as indicated in Figure 8. Positions are measured relative to the location of the label and north is up in all of the panels. Cuts *a* and *b* run along the ridges of the  $\text{NH}_3$  (1,1) emission. Cut *c* goes through emission to the west of the northern gap. Cuts *d* and *e* probe the high-velocity emission to the southwest of the CND. Cut *f* runs through the  $50 \text{ km sec}^{-1}$  cloud which borders Sgr A East in the north east.

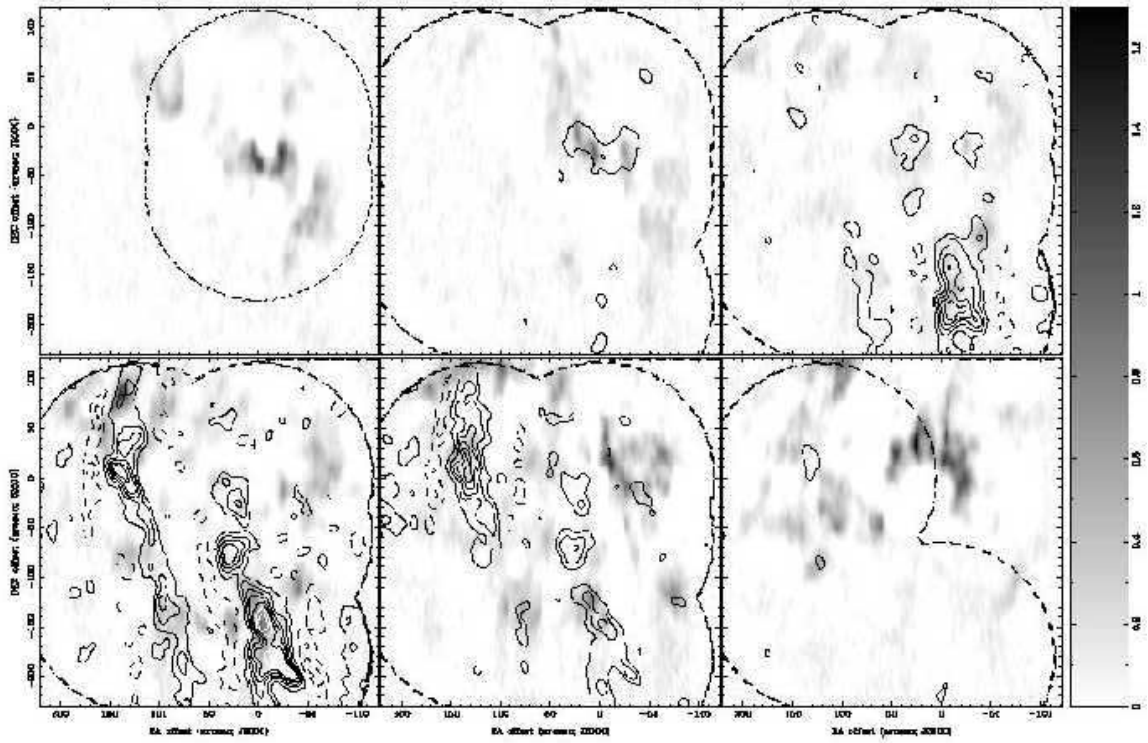


FIG. 14.— Comparison of HCN(1-0) (greyscale) and  $\text{NH}_3(1,1)$  (Coil & Ho 2000) (contours) in 6 velocity intervals: top left  $-75$  to  $-35$   $\text{km s}^{-1}$ , Top middle  $-35$  to  $-10$   $\text{km s}^{-1}$ , top right  $-10$  to  $15$   $\text{km s}^{-1}$ , bottom left  $15$  to  $40$   $\text{km s}^{-1}$ , bottom middle  $40$  to  $60$   $\text{km s}^{-1}$ , and bottom right  $60$  to  $100$   $\text{km s}^{-1}$ .

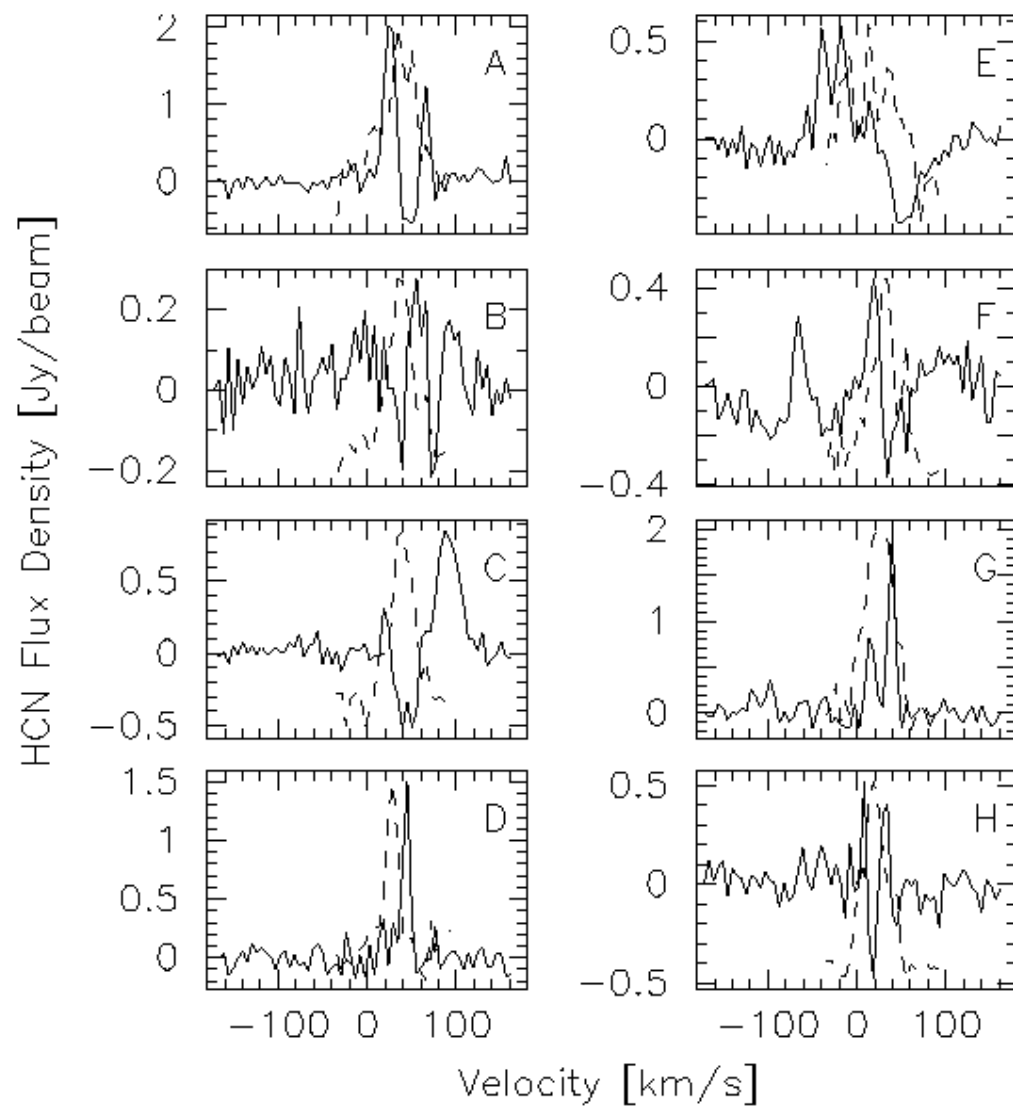


FIG. 15.— Spectra of HCN (solid lines) and NH<sub>3</sub>(1,1) (dashed lines) at the positions marked in Figure 14.

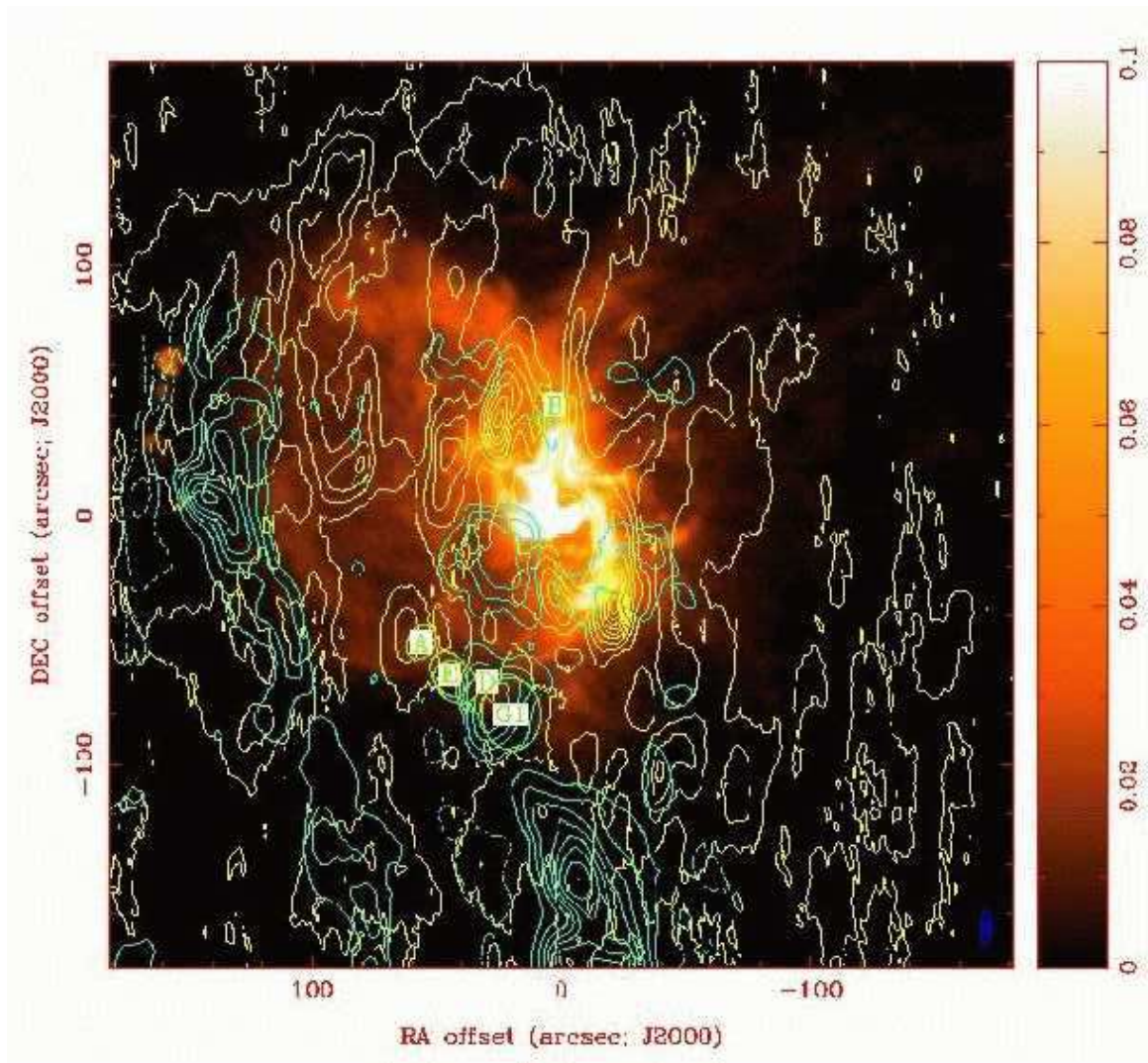


FIG. 16.— Comparison of HCN(1-0) (yellow contours) and NH<sub>3</sub>(1,1) (Coil & Ho 2000) (blue contours) in the velocity range  $-75$  to  $+55$  km  $s^{-1}$  overlaid on 6 cm continuum emission (color). Positions of OH masers (Yusef-Zadeh et al. 1999) are marked with letters.



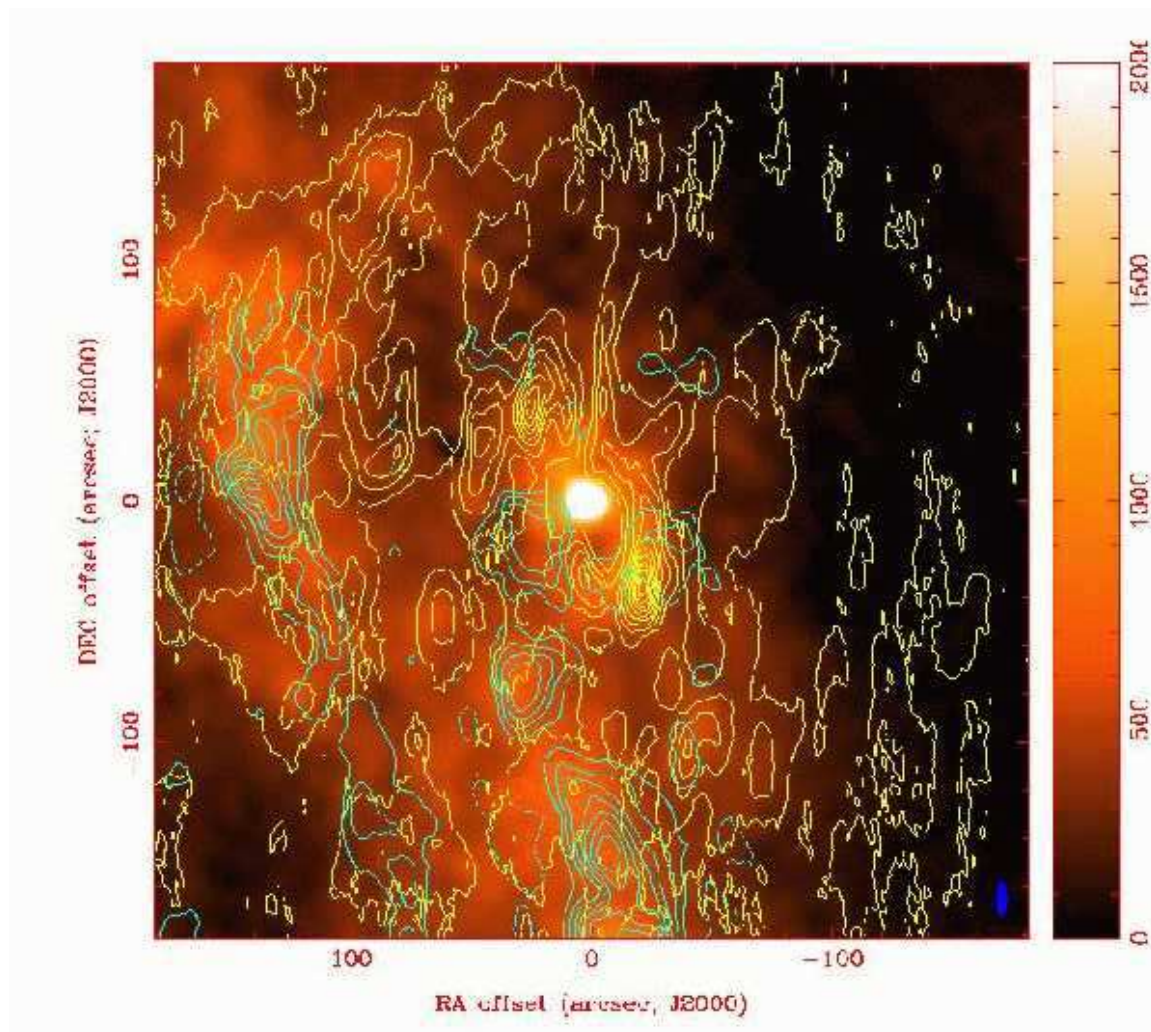


FIG. 17.— Comparison of HCN(1-0), 1.2mm continuum (Zylka 1998), and NH<sub>3</sub>(1,1). The 1.2 mm continuum (color background) largely traces dust. The HCN (yellow contours, levels .04, .125, .21, .29, .37, .47, .54, .62, .71, .78 Jy), is averaged over a 300 km s<sup>-1</sup> interval. NH<sub>3</sub>(1,1) emission (Coil & Ho 2000) (blue contours), is averaged over -40 to +55 km s<sup>-1</sup>.